JGR Atmospheres

RESEARCH ARTICLE
10.1029/2021JD035035

OCO-2 Satellite-Imposed Constraints on Terrestrial Biospheric CO_2 Fluxes Over South Asia

Sajeev Philip[1,2], Matthew S. Johnson[3], David F. Baker[4,5], Sourish Basu[6,7], Yogesh K. Tiwari[8], Nuggehalli K. Indira[9], Michel Ramonet[10], and Benjamin Poulter[6]

[1]NASA Academic Mission Services by Universities Space Research Association at NASA Ames Research Center, Mountain View, CA, USA, [2]Now at Centre for Atmospheric Sciences, Indian Institute of Technology Delhi, New Delhi, India, [3]Earth Science Division, NASA Ames Research Center, Moffett Field, CA, USA, [4]NOAA Earth System Research Laboratory, Global Monitoring Division, Boulder, CO, USA, [5]Cooperative Institute for Research in the Atmosphere, Colorado State University, Fort Collins, CO, USA, [6]NASA Goddard Space Flight Center, Greenbelt, MD, USA, [7]University of Maryland, College Park, MD, USA, [8]Indian Institute of Tropical Meteorology, Ministry of Earth Sciences, Pune, India, [9]CSIR Fourth Paradigm Institute (Formerly CSIR Centre for Mathematical Modelling and Computer Simulation), Bengaluru, India, [10]Laboratoire des Sciences du Climat et de l'Environnement, LSCE-IPSL (CEA-CNRS-UVSQ), Université Paris-Saclay, Gif-sur-Yvette, France

Key Points:

- Retrievals of column-averaged carbon dioxide from NASA's OCO-2 satellite are applied to constrain biospheric fluxes in South Asia
- The seasonal amplitude of South Asian biospheric fluxes were estimated to be larger than previously assumed for this region
- Biospheric CO_2 flux seasonality estimated by assimilating OCO-2 data compares favorably to independent measurements and satellite-based vegetation indices

Supporting Information:

Supporting Information may be found in the online version of this article.

Correspondence to:

M. S. Johnson and S. Philip,
matthew.s.johnson@nasa.gov;
philip.sajeev@gmail.com

Citation:

Philip, S., Johnson, M. S., Baker, D. F., Basu, S., Tiwari, Y. K., Indira, N. K., et al. (2022). OCO-2 satellite-imposed constraints on terrestrial biospheric CO_2 fluxes over South Asia. *Journal of Geophysical Research: Atmospheres*, *127*, e2021JD035035. https://doi.org/10.1029/2021JD035035

Received 9 APR 2021
Accepted 4 JAN 2022

Abstract The spatiotemporal variability of terrestrial biospheric carbon dioxide (CO_2) fluxes over South Asia has large uncertainty. The Orbiting Carbon Observatory 2 (OCO-2) satellite provides much-needed retrievals of column-average CO_2 on a global-scale, with the highest sensitivity to surface CO_2 fluxes and spatiotemporal resolution available to-date. This study conducted global inverse model simulations, assimilating in situ (IS) data and OCO-2 retrievals, to assess optimized CO_2 net ecosystem exchange (NEE) fluxes for South Asia. Annual Net Biome Exchange (NBE = NEE + biomass burning) fluxes over South Asia were estimated to be near neutral (0.04 ± 0.14 PgC yr^{-1}) using both IS and OCO-2 observations. The most robust result found by assimilating OCO-2 observations was the constraint imposed on the seasonal cycle of NBE fluxes. The amplitude of the seasonal cycle of NEE was found to be larger than previously assumed. The OCO-2 inversion led to an NBE seasonal amplitude of 0.34 PgC $month^{-1}$, which was larger compared to IS constrained NBE (0.19 PgC $month^{-1}$) and MsTMIP ensemble mean NEE (0.16 PgC $month^{-1}$). Moreover, OCO-2 data imposed a phase shift in the NBE seasonal cycle predicted by the prior model. The larger magnitude of NEE seasonality, and phase shift, simulated when assimilating OCO-2 observations are in general agreement with previous studies assimilating regional aircraft observations in addition to global IS observations. This result suggests that OCO-2 provides valuable data that allows for the estimate of NBE on a regional scale in a similar manner as regional in situ aircraft networks.

Plain Language Summary The terrestrial biosphere plays a significant role in the global carbon budget. As biosphere-atmosphere exchange is one of the largest sources of uncertainty in the global carbon cycle, it is important that we better understand the sources and sinks of biospheric carbon dioxide (CO_2). A major limitation for estimating CO_2 fluxes from the terrestrial biosphere has historically been the scarcity of measurement data. However, to alleviate this issue, NASA's Orbiting Carbon Observatory 2 (OCO-2) satellite was launched in 2014 with the goal to improve our understanding about the regional exchange of CO_2 between the terrestrial biosphere and atmosphere. This study applied OCO-2 data focusing on South Asia, a region with highly uncertain spatiotemporal variability of terrestrial biospheric fluxes. When using OCO-2 data in this study, a larger seasonal amplitude of biospheric CO_2 fluxes was estimated compared to what has previously been assumed for this region. A noticeable difference in the temporal variability of the CO_2 flux seasonality was also determined when using satellite data. The results of this study suggest that OCO-2 provides data sufficient for estimating biospheric CO_2 fluxes at a regional scale in a similar manner as regional aircraft networks.

1. Introduction

Nearly a quarter of the atmospheric carbon dioxide (CO_2) burden is controlled by terrestrial biospheric CO_2 fluxes, which are currently estimated to constitute a global sink of 3.4 ± 0.9 PgC yr^{-1} during the period of 2010–2019 (Friedlingstein et al., 2020; Schimel et al., 2001). Global biospheric CO_2 fluxes are comparatively

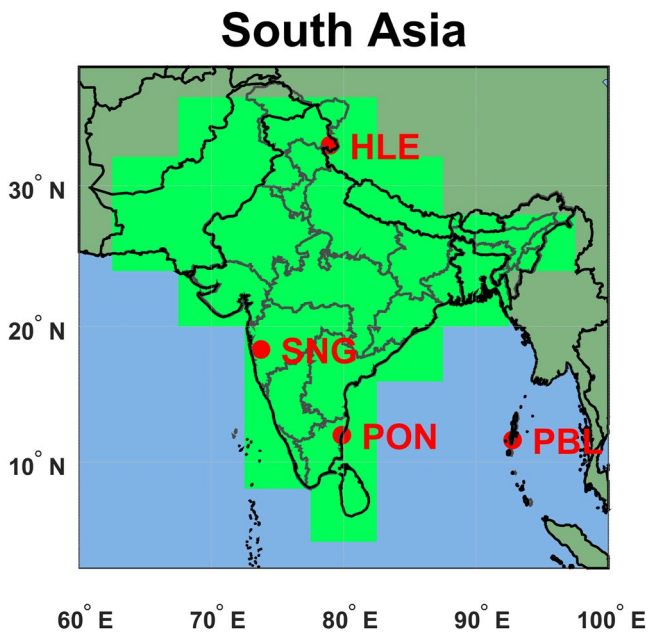

Figure 1. The South Asia region boundaries (light green) used to aggregate CO_2 fluxes. The locations of the four flask CO_2 measurement stations (Port Blair [PBL] Pondicherry [PON], Sinhagad [SNG], and Hanle [HLE]) are overlaid (red dots) for reference.

better constrained than regional-scale fluxes as large uncertainties still exist for regional estimates of land-air CO_2 exchange (Bastos et al., 2020; Schimel et al., 2015), especially over the tropical regions (Gaubert et al., 2019; Gurney et al., 2002; Peylin et al., 2013). Accurate regional-scale biospheric CO_2 flux estimates are essential for developing policies to mitigate rapidly increasing fossil fuel CO_2 emissions (Ciais et al., 2014; Friedlingstein et al., 2014; Peters et al., 2020). Atmospheric inverse models assimilating global in situ observations (Ciais et al., 2010; Peylin et al., 2013) and satellite column retrievals (Crowell et al., 2019; Houweling et al., 2015) are currently used to optimize global and regional CO_2 fluxes through "top-down" inversion frameworks (Newsam & Enting, 1988). However, the spatial and temporal gaps in observational data over certain regions impose uncertainties on regional-scale flux estimations (Byrne et al., 2017; Liu et al., 2014). South Asia (see Figure 1; defined as the region comprising India, Pakistan, Bangladesh, Nepal, Sri Lanka, and Bhutan) is such a region with sparse observations, which impedes the accurate quantification of regional CO_2 fluxes and seasonal variability of net ecosystem exchange (NEE) fluxes (Chakraborty et al., 2020; Patra et al., 2013; Thompson et al., 2016). "Bottom-up" NEE estimates from terrestrial ecosystem models also have uncertainty over South Asia (Patra et al., 2013), warranting further studies using ecosystem models, atmospheric inverse models and regional in situ atmospheric CO_2 mole fraction measurement data for this region. More measurement stations are fortunately currently being implemented over this region (e.g., Lin et al., 2015; Nalini et al., 2019; Tiwari et al., 2014) with a potential to better constrain regional CO_2 fluxes in the future.

Understanding the spatiotemporal variability of terrestrial biospheric CO_2 fluxes over South Asia is critical for assessing the global carbon cycle (Peylin et al., 2013). This is due to the unique features of this particular region, with distinct Asian monsoonal weather systems influencing biospheric CO_2 flux exchange and atmospheric CO_2 concentrations (e.g., Bhattacharya et al., 2009; Ravi Kumar et al., 2016; Schuck et al., 2010; Tiwari et al., 2014; Tiwari, Revadekar, & Ravi Kumar, 2013; Valsala et al., 2013), uncertain impacts from El Niño–Southern Oscillation (ENSO) cycling (Liu et al., 2017), and steadily increasing fossil CO_2 emissions over the last two decades (Friedlingstein et al., 2020). Previous top-down estimates from an ensemble of inverse models show that the South Asian terrestrial biosphere is either carbon neutral (Thompson et al., 2016) or a small sink (e.g., Niwa et al., 2012; Patra et al., 2011; Swathi et al., 2021). Bottom-up ecosystem models predicted a small sink over South Asia during recent years (e.g., Gahlot et al., 2017; Patra et al., 2013; Sitch et al., 2015), and a small source over India during the 1901–2010 period (Rao et al., 2019). An ensemble of top-down and bottom-up flux estimates assessed by Patra et al. (2013) found large variability in the estimates of NEE seasonal cycle, with ensemble members predicting peak CO_2 emissions ranging from March to July, and peak uptake ranging from August to October. Three studies (Jiang et al., 2014; Niwa et al., 2012; Patra et al., 2011) assimilating in situ data from regional passenger aircraft networks (Civil Aircraft for the Regular Investigation of the atmosphere Based on an Instrument Container project [CARIBIC; Brenninkmeijer et al., 2007] and Comprehensive Observation Network for Trace gases by AIrLiner project [CONTRAIL; Machida et al., 2008]) also displayed differences among them in estimating the seasonal amplitude, and the timing of peak CO_2 source and sink (further described in Section 4.3).

Most of the past research efforts focusing on NEE in South Asia lacked regional observations; therefore, further studies are needed to understand the inter-annual variability, amplitude, and phase of the seasonal cycle of biospheric CO_2 fluxes in this region. The discrepancies in CO_2 flux seasonality as estimated by previous studies (Patra et al., 2013) could be largely due to the scarcity of surface and airborne CO_2 observations over this region. Therefore, satellite retrievals of atmospheric column-average CO_2 dry-air mole fraction (XCO_2) data could compensate for the lack of in situ (IS) observations to help constrain South Asian NEE estimates. Assimilating satellite XCO_2 retrievals rather than IS CO_2 observations can also be more advantageous because of the lower sensitivity of column data assimilations to model transport errors, as compared to IS data assimilations (Basu et al., 2018; Crowell et al., 2019; Rayner & O'Brien, 2001).

Table 1
Details of Specific Terms Used in This Study

Specific terms used	Details
Terrestrial biospheric flux	NBE (= NEE + BBE)[a]
Net CO_2 flux[b]	NBE + fossil fuel + oceanic flux
Seasonal amplitude	Absolute magnitude of the difference between the maximum and minimum of monthly mean values
Multi-year monthly mean	Mean of monthly flux for 2015–2018
SD of monthly NBE[c]	Standard deviation of monthly NBE for 2015–2018
Multi-year mean NBE	Mean of annual NBE values for 2015–2018
Annual NBE anomaly	Annual NBE minus multi-year mean NBE

[a]NEE, BBE, and NBE refer to net ecosystem exchange flux, biomass burning emissions, and net biome exchange (NEE + BBE), respectively. [b]The net flux over South Asia is the sum of NBE and fossil fuel emissions as no ocean grids are included in the South Asian terrestrial region. [c]*SD* of monthly NBE reflects the inter-annual spread in the monthly mean values.

The Orbiting Carbon Observatory 2 (OCO-2) satellite provides global retrievals of XCO_2 starting from 6 September 2014. To date, OCO-2 is the sensor with the highest spatial resolution (~3 km^2) and highest sensitivity to surface level CO_2 (Crisp et al., 2017) which aids to improve the current understanding of CO_2 surface fluxes (e.g., Eldering et al., 2017; Liu et al., 2017). An ensemble of top-down global surface CO_2 flux estimates based on different inverse modeling systems were conducted by Crowell et al. (2019) using version 7 OCO-2 retrievals. Crowell et al. (2019) reported larger NEE seasonal cycle amplitudes over the Northern Tropical zonal band (defined as 0°–23°N; which comprises the majority of the South Asia region considered in this study; see Figure 1) when constrained by OCO-2, compared to prior biospheric models and IS-based inversions. This larger Northern Tropical land flux seasonality estimated by OCO-2 data is in agreement with estimates derived by assimilating data from the Greenhouse gases Observing SATellite (GOSAT) instrument (Palmer et al., 2019). Over Tropical Asia (region 9 defined by the TransCom-3 project), GOSAT-based inversions revealed stronger seasonality in NEE fluxes compared to surface data inversions (Basu et al., 2014). Since Crowell et al. (2019) was published, version 9 of the OCO-2 retrieval data has become available up to 2019. This version includes improvements to the retrieval algorithm and bias corrections (Kiel et al., 2019; O'Dell et al., 2018) enabling the better quantification of global and regional surface CO_2 fluxes (Miller & Michalak, 2020). This study is therefore designed to assess inverse model fluxes using OCO-2 version 9 retrievals in a sub-region of the Northern Tropical land (South Asia) for the first time.

The objective of this study was to report and analyze the constraints imposed by OCO-2 column retrievals on the annual mean, interannual variability, and seasonal cycle of South Asian terrestrial biospheric CO_2 fluxes. For this we conducted global inverse model simulations using OCO-2 XCO_2 and global IS observations as part of the second OCO-2 Multi-model Intercomparison Project (MIP) using version 9 of the OCO-2 retrievals (hereafter OCO-2 v9 MIP). We organize the paper in the following way. Section 2 presents the assimilated observations, evaluation datasets, and vegetative indices used for validation. The flux inversion framework and evaluation methodology are described in Section 3. We present the evaluation of the flux inversion system using global and regional observations, analysis of the South Asian biospheric fluxes, and comparison of fluxes with satellite-derived vegetation indices and previous publications in Section 4. Finally, Section 5 presents our concluding remarks. Table 1 shows details of specific terms used in the following sections.

2. Data

The four-dimensional variational (4D-Var) assimilation system with the GEOS-Chem global chemical transport model (CTM; Philip et al., 2019) was used to estimate global NEE and oceanic CO_2 fluxes on a monthly scale at the spatial resolution of the model from 2015 to 2018 (see Section 3). Regionally aggregated NEE and Net Biome Exchange (NBE = NEE + unoptimized biomass burning emissions [BBE]) fluxes over the South Asia region were assessed. We also conducted an evaluation of the global inversion system using independent observation datasets on a global-scale and unassimilated observations over South Asia. Furthermore, monthly mean NBE is compared with satellite-based vegetative indices (see Section 2.3) to help interpret the observed seasonal cycle.

The following section describes the observational data used in the data assimilation system (Section 2.1), unassimilated observations used to perform an independent evaluation of the optimized fluxes (see Section 2.2) and satellite-based vegetative indices used to compare with NEE flux seasonality (Section 2.3).

2.1. Assimilated Data

2.1.1. OCO-2 Retrievals

The OCO-2 satellite follows a sun-synchronous polar orbit along the Afternoon Constellation (A-train) of Earth Observing Satellites (EOS), providing retrievals on a global scale with a local satellite overpass time of ~1:30 pm (Crisp et al., 2017). The observing modes of OCO-2 soundings considered in this study are Land Nadir (LN) and Land Glint (LG). We do not report on assimilations using the OCO-2 Ocean Glint observing mode due to unresolved biases in the retrievals (personal communication from the OCO-2 science team; Crowell et al., 2019). We use the version 9 OCO-2 retrieval product (O'Dell et al., 2018) as applied in the OCO-2 v9 MIP. Because high spatiotemporal resolution OCO-2 soundings do not offer independent pieces of information to global flux inversion systems with coarse spatial resolutions, 10-s OCO-2 XCO_2 averages of individual soundings were calculated. OCO-2 data retrieval error and model representation error were also calculated, and reported along with each 10-s data (Baker et al., 2021; Basu et al., 2018; Crowell et al., 2019).

2.1.2. Global CO_2 In Situ Measurements

Global atmospheric CO_2 concentration measurements used for IS assimilation were compiled for the OCO-2 v9 MIP as an Observation Package (ObsPack) Data Product (Masarie et al., 2014) by the National Oceanic and Atmospheric Administration (NOAA) Earth Systems Research Laboratory (ESRL). ObsPack presents calibrated CO_2 measurements from different observing platforms, such as surface flasks, tall towers, and aircrafts operated by numerous institutes in a common format. For this study, we applied ObsPack data derived for the OCO-2 v9 MIP (Peiro et al., 2021). We assimilated ObsPack measurements which were flagged as "assimilable" by a prior run of NOAA's CarbonTracker data assimilation system. Individual assimilable ObsPack measurements were provided with measurement error terms, referred to as the Model-Data Mismatch (MDM). An empirical method known as an "adaptive model-data mismatch scheme" was used to calculate MDM values for each measurement as described in CarbonTracker CT2019 documentation.

2.2. Evaluation Data

2.2.1. Withheld Global CO_2 Measurements

For the OCO-2 v9 MIP, ~3% of the ObsPack data were randomly selected and withheld (not assimilated in IS model simulations) for cross-evaluation of the inverse model optimized atmospheric CO_2 concentrations. The selection scheme for withheld data was designed to make the withheld measurements as independent as possible from assimilated measurements (see details in CarbonTracker CT2019 documentation). The withheld ObsPack dataset were also provided with a valid MDM value for each measurement in order to evaluate model CO_2 fields by considering the errors in the measurement data.

2.2.2. Unassimilated Data Over South Asia

We used observations from four surface IS CO_2 measurement stations in and around the South Asia region, which are not assimilated in the inverse model simulations, to serve as an independent evaluation data source. The stations provided surface CO_2 flask measurements taken from Port Blair (PBL; marine site), Pondicherry (PON; coastal site), and Hanle (HLE; mountain site) locations operated by the Council of Scientific and Industrial Research Fourth Paradigm Institute (CSIR-4PI, India), with analysis by the Laboratoire des Sciences du Climat et de l'Environnement (LSCE, France; Lin et al., 2015). We also used data from the Sinhagad station (SNG; a mountain site) operated by the Indian Institute of Tropical Meteorology, India (Tiwari et al., 2014). These flask measurements from all four monitoring stations (see locations in Figure 1) were calibrated against WMOX2007 standards (Lin et al., 2015, 2018).

2.3. Satellite-Derived Vegetation Indices

For comparing vegetation indices against prior and optimized NEE fluxes over South Asia, we regridded the following data from their native spatiotemporal resolution into the spatial resolution of the atmospheric transport model (4.0° × 5.0° latitude × longitude) on a monthly scale from 2015 to 2018.

2.3.1. NDVI and EVI

In order to assess the photosynthetic capacity of the South Asian terrestrial biosphere, we use satellite-retrieved vegetative indices, such as the Normalized Difference Vegetation Index (NDVI) and Enhanced Vegetation Index (EVI; Huete et al., 2002; Tucker et al., 1986). NDVI is derived from satellite-retrieved surface reflectance in near-infrared (841–876 nm) and red (620–670 nm) wavelength bands, whereas EVI uses an additional blue (459–479 nm) channel (Huete et al., 2002) to account for water vapor absorption. The NDVI and EVI data were collected from the Moderate Resolution Imaging Spectroradiometer (MODIS) instrument on the Terra satellite (MOD13C2 Climate Modeling Grid (CMG) Version 6). MODIS NDVI and EVI Level 3 products are at the spatial resolution of 0.05° × 0.05° and are provided at a 16-day temporal average. We retain data flagged as "good data" or "marginal data" by the pixel reliability index. Because the prior biosphere model used in this study (see Section 3.2) was driven with NDVI retrieved from the Advanced Very High Resolution Radiometer (AVHRR) satellite, we also use the NOAA Climate Data Record AVHRR NDVI Version 5 product (Vermote, 2019) to inter-compare with MODIS products. The AVHRR NDVI product is at a spatial resolution of 0.05° × 0.05° and daily temporal frequency. We avoided data marked by quality assessment flags as "pixels with cloudy, containing cloud shadow, over water, over sunglint and at night, and channel 1 or 2 are invalid".

2.3.2. Solar Induced Fluorescence (SIF)

Satellite retrievals of SIF were also used to investigate the biospheric photosynthetic activity in the South Asia region. We used SIF products based on retrievals from the OCO-2 satellite (Sun et al., 2018). This spatially contiguous SIF data, at a spatial resolution of 0.05° × 0.05° and a temporal resolution of 16 days, were derived by training the native discontinuous SIF data from OCO-2 and surface reflectance data from MODIS, in a machine learning algorithm (Yu et al., 2019a, 2019b). This SIF product was derived using a combination of retrievals at two wavelengths: 757 and 771 nm, respectively (Yu et al., 2019b). We also use the version 28 SIF product from the Global Ozone Monitoring Experiment 2 (GOME-2) instrument onboard the MetOp-B satellite (Joiner et al., 2013, 2014, 2016). Note that GOME-2 has an overpass time around 9:30 am at the equator and SIF was retrieved at 740 nm. The GOME-2 SIF product is at a spatial resolution of 0.5° × 0.5° and monthly temporal resolution.

3. Model Framework

We conducted a series of global inverse model simulations, and subsequent evaluation of the posterior fluxes, to assess the optimized NEE aggregated over South Asia. The horizontal resolution of the model is 4.0° × 5.0°, which results in 29 grid box values over the South Asia region (see Figure 1). Note that several previous studies employed the same practice of conducting global assimilations and aggregating optimized gridded fluxes to specific regions (e.g., TransCom-3 regions) to assess regional-scale fluxes (e.g., Basu et al., 2014; Niwa et al., 2012; Patra et al., 2011; Swathi et al., 2021; Thompson et al., 2016). The advantages of employing a global inversion system for this purpose includes a consistent simulation of atmospheric CO_2 growth rate and global CO_2 flux budget, and the elimination of errors in boundary/initial conditions inherent in regional model simulations. We recognize that assimilating satellite column data at a finer spatial resolution (finer than 1° × 1° spatial resolution) using regional model simulations (e.g., Villalobos et al., 2021) might better optimize fluxes over a small region. However, using regional inversions to invert full-column satellite CO_2 data is known to be problematic, due to the large fraction of the signal in the full column measurements caused by fluxes outside the regional domain being uncorrected in the regional inversion.

Inverse model simulations were conducted by assimilating OCO-2 XCO_2 retrievals and global IS observations following the protocols of the OCO-2 v9 MIP. Flux inversions were conducted for the years 2015–2018 by assimilating observations from 6 September 2014 to 31 May 2019. As part of the OCO-2 v9 MIP, we assimilated different observational modes separately and in various combinations. However, in this study we focused on inversions assimilating IS data (IS-based inversion) and OCO-2 LN + LG (hereafter "OCO-2 inversion" refers to

the simulation using just the OCO-2 LN + LG observational mode data). OCO-2 data outside of the 66°N–66°S band were not assimilated. We do not estimate posterior error covariance for the OCO-2 MIP experiments, since posterior uncertainly estimations (e.g., Bousserez et al., 2015; Liu et al., 2014) are typically not highly reliable and also computationally expensive. Instead, for the OCO-2 v9 MIP, the posterior uncertainty is typically represented by the standard deviation of an ensemble of inversions (Crowell et al., 2019). The following sections describe the flux inversion framework and evaluation approach.

3.1. GEOS-Chem Model

The CO_2 flux inversion system in this study uses the GEOS-Chem CTM to simulate the transport of CO_2 (Bey et al., 2001; Nassar et al., 2010; Suntharalingam et al., 2004). For posterior flux calculations, we use the GEOS-Chem adjoint, version 35a (Henze et al., 2007; Liu et al., 2014). The GEOS-Chem forward model (e.g., Krishnapriya et al., 2020; Nassar et al., 2010) and GEOS-Chem-based 4D-Var data assimilation system have been extensively validated and used for CO_2 flux inversions in previous studies (e.g., Bowman et al., 2017; Deng et al., 2014; Liu et al., 2017; Philip et al., 2019; Wang et al., 2019). In this study, MERRA-2 assimilated meteorology was used to drive the forward model. The MERRA-2 fields were originally at native $0.5° \times 0.625°$ horizontal grids and 72 vertical layers. In order to attain reasonable computational speed, we conduct simulations with low spatial resolution of $4.0° \times 5.0°$ horizontal grids with 47 vertical layers.

3.2. Prior CO_2 Fluxes

In order to provide prior fluxes in the inversion system, we apply fossil fuel usage, oceanic, NEE, and BBE fluxes. Hourly fossil fuel data is derived from the Open-source Data Inventory for Anthropogenic CO_2 (ODIAC; Oda et al., 2018), by extrapolating ODIAC beyond year 2017 with world energy statistics, and imposing diurnal and weekday/weekend variability based on Nassar et al. (2013). The oceanic, NEE and BBE fluxes generated as a prior for the CarbonTracker 2019 (CT2019) data assimilation system (Peters et al., 2007) were used as prior fluxes in this study. These first-guess fluxes from CT2019 were year-specific and at 3-hr temporal resolutions. These products were regridded from native spatial resolutions to the $4.0° \times 5.0°$ resolution of the GEOS-Chem model. We use the CT2019 unoptimized three-hourly oceanic CO_2 fluxes from the Ocean Inversion Fluxes prior (OIF) product described by Jacobson et al. (2007, 2020) and CarbonTracker CT2019 documentation). Prior NEE fluxes were from the CT2019 CASA-Global Fire Emissions Database version 4.1s (CASA-GFED4.1s) biosphere model (Giglio et al., 2006; Potter et al., 1993; van der Werf et al., 2003, 2006). The three-hourly NEE fluxes were generated by imposing diurnal variability and monthly smoothing to the monthly NEE from the CASA-GFED4.1s model (Jacobson et al., 2020; Olsen & Randerson, 2004). The NDVI data from the AVHRR satellite was used to drive the CASA-GFED4.1s model. Note that due to data availability, NEE data for 2018 were set equal to those of 2017. Biomass burning fluxes were derived from the CT2019 CASA-GFED4.1s module (Giglio et al., 2013; van der Werf et al., 2010, 2017) with scaling factors (Mu et al., 2011) applied on monthly data to generate three-hourly fluxes. Fire count data from the MODIS satellite were used to calculate burned area in GFED4.1s. Compared to earlier versions of GFED, the latest GFED4.1s version contains carbon emission from small fires (van der Werf et al., 2017).

Table 2 shows the global CO_2 flux budgets averaged over the years 2015–2018. The prior net (sum of all sources) global annual mean CO_2 flux of 5.65 PgC agrees with an observation-based estimate of global annual net CO_2 flux of 5.50 ± 0.15 PgC over the period 2015–2018. The observation-based estimate of global annual net CO_2 flux over the period 2015–2018 was calculated by multiplying the CO_2 concentration growth rate of 2.59 ± 0.07 ppm (as documented at NOAA-ESRL) with a scale factor of 2.124 PgC ppm^{-1}, as suggested by Ballantyne et al. (2012).

3.3. Flux Inversion Framework

The 4D-Var data assimilation system with the GEOS-Chem CTM was used to conduct the CO_2 surface flux estimations following Philip et al. (2019). The inversion system minimizes the cost function (Equation 1) iteratively to optimize the state vector, $\boldsymbol{\sigma}$ representing scaling factors to be multiplied with monthly NEE and oceanic fluxes in surface grid boxes of the model ($\mathbf{x}$),

Table 2
Prior and Posterior Global and South Asian Annual CO_2 Flux Budgets (PgC yr^{-1}) Averaged From 2015 to 2018

	Global CO_2 budget (PgC yr^{-1})						South Asia CO_2 budget (PgC yr^{-1})				
	Fossil	BBE	NEE	NBE	Ocean	Net[a]	Fossil	BBE	NEE	NBE	Net[b]
Prior	10.05	1.59	−2.47	−0.88 ± 0.42[c] (*−1.20 ± 5.64*)[d]	−3.52 ± 0.12 (*−2.55 ± 0.99*)	5.65 (*6.28 ± 5.76*)	0.80	0.01	−0.02	−0.01 ± 0.03[c] (*−0.01 ± 0.54*)	0.79 (*0.79 ± 0.54*)
IS	10.05	1.59	−3.86	−2.28 ± 0.94 (*−2.64 ± 2.85*)	−2.45 ± 0.26 (*−2.10 ± 0.54*)	5.32 (*5.29 ± 3.02*)	0.80	0.01	0.03	0.04 ± 0.14 (*−0.07 ± 0.68*)	0.84 (*0.73 ± 0.68*)
OCO-2	10.05	1.59	−2.28	−0.70 ± 0.58 (*−1.39 ± 2.07*)	−4.01 ± 0.30 (*−3.28 ± 1.36*)	5.35 (*5.35 ± 2.51*)	0.80	0.01	0.03	0.04 ± 0.14 (*−0.08 ± 0.54*)	0.84 (*0.73 ± 0.54*)

[a]Net flux includes NBE, oceanic, and fossil fluxes. [b]Net flux over South Asia has no oceanic fluxes. [c]Uncertainty values for prior NBE and oceanic fluxes represent the standard deviations of multi-year mean values. Whereas, global annual total 1σ prior uncertainties for NEE and oceanic fluxes assumed in the inversion are ∼0.7 and ∼0.3 PgC $yr^{-1}$for each year, respectively (Section 3.4). The prior NEE uncertainty assumed over South Asia region is ∼0.14 PgC yr^{-1} for each year. [d]Values within the parenthesis and italics refers to ensemble mean from the OCO-2 v9 MIP product.

$$J(\sigma) = \frac{1}{2}(H(\sigma) - \mathbf{y})^T \mathbf{O}^{-1}(H(\sigma) - \mathbf{y}) + \frac{1}{2}(\sigma - \sigma_a)^T \mathbf{P}^{-1}(\sigma - \sigma_a) \quad (1)$$

where σ_a represents the prior scaling factors (unity) applied to the prior NEE and oceanic fluxes, and **y** is the vector of IS data and OCO-2 XCO_2 retrievals over the assimilation time-period. The construction of observational error covariance (**O**) and prior error covariance (**P**) are discussed in Sections 3.4 and 3.5, respectively. The observation operator (H) represents the model-simulated values corresponding to each observational data, **y**. The model-simulated XCO_2 corresponding to each OCO-2 data (H) is calculated by convolving the model CO_2 profile with the OCO-2 column averaging kernel vector (**a**),

$$H = XCO_{2(a)} + \mathbf{a}^T(\mathbf{f}(\sigma(\mathbf{x})) - \mathbf{c}_a) \quad (2)$$

where $\mathbf{f}(\boldsymbol{\sigma}(\mathbf{x}))$ is the model-simulated vertical profile of CO_2 interpolated to the retrieval levels of OCO-2. The prior vertical profile of CO_2 ($\mathbf{c}_a$) and the prior column CO_2 ($XCO_{2(a)}$) represent prior information used in the OCO-2 XCO_2 retrieval process (O'Dell et al., 2012).

Oceanic CO_2 and NEE fluxes were optimized at a monthly temporal resolution, whereas fossil fuel and biomass burning CO_2 emissions were kept unoptimized. The diurnal variability of prior NEE and oceanic fluxes was included (see Section 3.2) to drive diurnally varying atmospheric CO_2 concentrations in the model; however, the NEE and oceanic fluxes were optimized on a monthly timescale. In order to reduce the computation time necessary for running 4 yr of simulations, we conduct four parallel inversions for each year from 2015 to 2018. Simulations for each year started from September 1 of the previous year, and ended in March of the following year (end date is 31 May 2019 for the simulation year 2018). Therefore, the assimilation window is 19 months (21 months for the simulation year 2018) with 4 months of spin-up and 3 months (5 months for the simulation year 2018) of spin-down time. For conducting these four parallel inversions for years 2015–2018, we use initial atmospheric concentrations of CO_2 on September 1 for 2014–2017. The initial concentration for 1 September 2014 were generated by running the GEOS-Chem forward model following Philip et al. (2019). Data for September 1 corresponding to years 2015 to 2017 were calculated by upscaling previous year's values by 0.75% to account for annual growth rate in atmospheric CO_2 mole fraction. Four months of spin-up time for each simulation was chosen to minimize the impact of initial CO_2 concentration on optimized surface fluxes. This model configuration was thoroughly tested using Observing System Simulation Experiments as described in Philip et al. (2019).

3.4. Prior Flux Uncertainty

The prior flux error covariance (**P**) of NEE and oceanic fluxes were assigned as follows. Spatial and temporal correlations in the **P** matrix implemented in some 4D-Var inversion systems (e.g., Basu et al., 2013; Chevallier et al., 2010) were ignored during this study considering the coarse resolution of the model used here (e.g., Baker et al., 2010; Deng et al., 2014; Liu et al., 2014). Oceanic prior flux error was assigned to be five times the absolute value of monthly oceanic prior fluxes in each surface grid box of the model, in order to account

for error correlations. This corresponds to a global 1σ uncertainty of ~0.3 PgC yr^{-1} for each year. The scaling factor was chosen to produce global oceanic uncertainty totals in accordance with the Global Carbon Project (GCP) for the years 2015–2018 (Friedlingstein et al., 2019). The prior NEE flux error is calculated as the range (difference of flux minimum and maximum) of five different biosphere models (CT2019-CASA-GFED4.1s, Lund-Potsdam*Jena [LPJ; Poulter et al., 2014; Sitch et al., 2003], CASA-GFED3 [Potter et al., 1993; Randerson et al., 1996; van der Werf et al., 2004, 2010], NASA-CASA [Potter et al., 2003, 2007, 2009; Potter, Klooster, & Genovese, 2012; Potter, Klooster, & Genovese, Hiatt, et al., 2012)], and Simple-Biosphere model version 4 [SiB-4; Denning et al., 1996; Haynes, et al., 2019; Sellers et al., 1986]), applying a scaling factor of 1.35 to represent unaccounted-for uncertainty components and keeping an upper bound of five times the absolute value of monthly prior NEE range for each model grid cell. This approach of scaling NEE range with 1.35 (and adding an upper bound of five times prior NEE) leads to a global NEE flux 1σ uncertainty of ~0.7 PgC yr^{-1}, so that the global annual total uncertainties are generally in agreement with estimates from the GCP for years 2015–2018. The GCP calculated uncertainties are 0.7–1.0 PgC yr^{-1} for the terrestrial biospheric CO_2 fluxes and 0.5–0.6 PgC yr^{-1} for the oceanic CO_2 fluxes (Friedlingstein et al., 2019). Since the GEOS-Chem 4D-Var system optimizes scaling factors (Section 3.3), the fractional error was calculated by taking the ratio of absolute prior NEE flux error to the absolute value of the NEE flux magnitude, and the square of the fractional error was assigned as the diagonal elements of the **P** matrix.

3.5. Observational Uncertainty

The observational error covariance matrix (**O**) was specified corresponding to the assimilated in situ CO_2 concentrations and OCO-2 XCO_2 column retrievals following OCO-2 v9 MIP protocols. No observation error correlations between individual IS or 10-s-averaged OCO-2 data were applied in this study, although error correlations were accounted for in calculating the uncertainties placed on the 10-s OCO-2 data (Baker et al., 2021). The MDM values estimated for each IS observation were used in the observational error covariance for IS data. We used the quadratic sum of the OCO-2 10-s data retrieval error and model representation error to construct the **O** matrix when assimilating OCO-2 XCO_2 data (from variables "xco2_uncertainty" and "model_error" in file OCO2_b91_10sec_GOOD_r24.nc4).

3.6. Evaluation of the Flux Inversions

Prior and optimized CO_2 fluxes were evaluated indirectly by comparing the prior and posterior CO_2 atmospheric concentration fields against several global observational datasets and unassimilated observations from four stations over South Asia (see Figure 1). The prior and posterior model CO_2 concentrations and XCO_2 values were calculated by conducting forward model simulations using the prior and optimized fluxes, respectively, and sampling the model at the spatiotemporal frequency of the observational data. We compare the prior and optimized model CO_2 fields against (a) withheld ObsPack IS CO_2 mixing ratio observations, (b) assimilated ObsPack data, and (c) assimilated OCO-2 XCO_2 (LN and LG data). The comparison of inversions against withheld ObsPack data can be considered fully independent.

The statistical parameters used for model evaluation are normalized mean bias (NMB), standard deviation of the error (SDE), root mean square error (RMSE), and correlation coefficient (R). While calculating NMB by comparing model simulated CO_2 fields (SIM) against ObsPack and OCO-2 observations (OBS), we normalize them by the observational error values (MDM) reported for each observation,

$$\mathrm{NMB} = \frac{\sum_{i=1}^{N} \left(\frac{\mathrm{SIM_i} - \mathrm{OBS_i}}{\mathrm{MDM_i}} \right)}{N} \tag{3}$$

where N is the total number of observations. Observational error values (MDM) were available for ObsPack and OCO-2 data. The error term RMSE is defined as follows:

$$\mathrm{RMSE} = \sqrt{\frac{\sum_{i=1}^{N} (\mathrm{SIM_i} - \mathrm{OBS_i})^2}{N}} \tag{4}$$

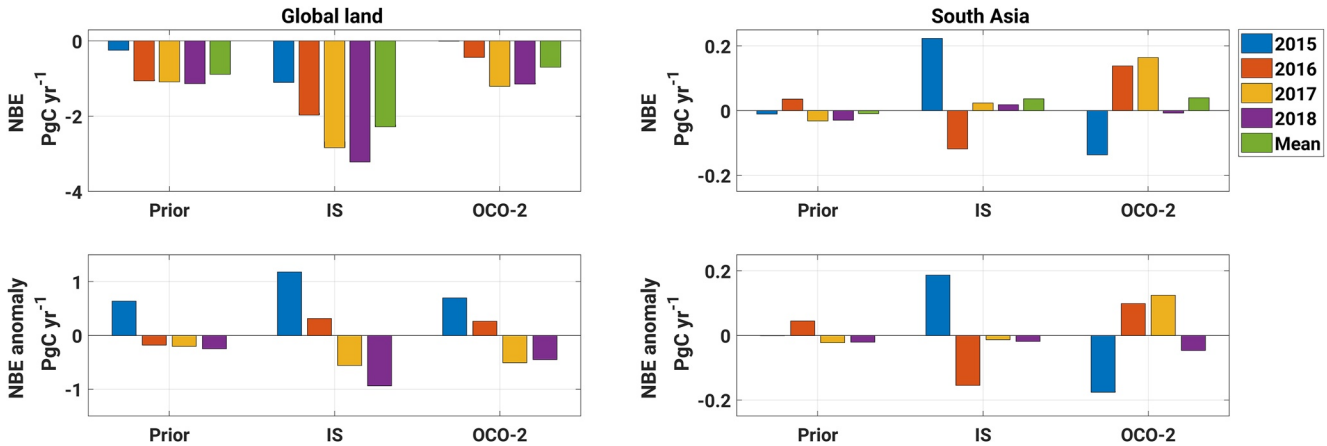

Figure 2. Annual and multi-year mean NBE (PgC yr^{-1}, top panels) and annual NBE anomalies (PgC yr^{-1}, bottom panels) over the global land (left column) and South Asia region (right column) corresponding to the prior model and posteriors optimized with IS and OCO-2 LN + LG observations (as shown in the *x*x-axis of each panel). Legends show the color of each bar representing annual and multi-year mean values.

The accuracy, precision, and uncertainty of the optimized CO_2 fields can be assessed by evaluation metrics NMB (or MB), SDE, and RMSE, respectively (see Vermote & Kotchenova, 2008). When using data other than the IS data collected in the South Asia region for the evaluations, we calculate statistics over the entire globe. Complete validation of this inversion system by comparison against individual data streams (e.g., flask vs. aircraft), validation of optimized CO_2 fields over individual regions or latitudinal bands, and over individual monitoring stations and campaigns, and comparison against other inverse models are conducted as part of the OCO-2 v9 MIP efforts. The validation statistics can be accessed from the OCO-2 v9 MIP website.

4. Results

4.1. Global CO_2 Flux

Table 2 shows the multi-year mean global budget of the prior and posterior (IS and LN + LG) CO_2 fluxes, and corresponding ensemble mean and *SD* from the OCO-2 v9 MIP (values taken OCO-2 v9 MIP website). The optimized net global multi-year mean fluxes (~5.35 PgC) are lower than the prior budget (5.65 PgC) but are still in agreement with observation-based estimate of global annual net CO_2 flux over the period 2015–2018 (5.50 ± 0.15 PgC; see Section 3.2). The partitioning of global land versus global ocean fluxes shows significant differences for OCO-2 versus IS-constrained fluxes, with OCO-2 observations leading to a smaller land sink (NBE = −0.70 PgC yr^{-1}) compared to the IS-based inversion (NBE = −2.28 PgC yr^{-1}). The OCO-2 v9 MIP ensemble mean also depicts similar differences in land-ocean flux partitioning while assimilating OCO-2 versus IS data (see Table 2). The large spread (*SD*) in the posterior NBE and ocean flux estimates in the OCO-2 v9 MIP reveals that different transport models fit IS and column XCO_2 data differently. In general, Table 2 shows that all the flux estimates (NEE, NBE, ocean, and net values) from the model are within the spread (SD) of OCO-2 v9 MIP ensemble mean values.

Figure 2 shows annual mean and multi-year mean NBE (and anomalies) over the global land. Both IS and OCO-2 observations produced global land CO_2 sinks during 2015–2018 (negative NBE values). Annual NBE anomaly signals varied between years, with positive anomaly values for 2015–2016 and negative anomaly values for 2017–2018. The prior model shows small negative annual NBE anomalies for all years except for 2015. The higher NBE anomaly values for 2015–2016 revealed by top-down estimates likely reflects the impact of the 2014–2016 El Niño event which led to reduced CO_2 uptake by the tropical terrestrial biosphere during the dry and hot months (Bastos et al., 2018; Liu et al., 2017; Patra et al., 2017). Figure S1 in Supporting Information S1 shows the seasonal variation of global land NBE, which is consistent with Crowell et al. (2019) and the OCO-2 v9 MIP results. Prior, and IS- and OCO-2-constrained global NBE fluxes display similar seasonal cycles with a large CO_2 land sink between May and August, and a moderate source in the remaining months.

Table 3
Comparison of Multi-Year Mean NBE Over South Asia Obtained in This Study With Other Studies

Study	Data assimilated	Years considered	NBE budget (PgC yr^{-1})[a]	Other details
Bottom-up				
Ciais et al. (2020)[b]	–	2000–2009	*−0.25 ± 0.11*	Ensemble of models
Cervarich et al. (2016)	–	2000–2013	*−0.22 ± 0.15*	Ensemble of models
Patra et al. (2013)	–	2000–2009	*−0.19 ± 0.19*	Ensemble of models
Gahlot et al. (2017)	–	2000–2012	*−0.02*	Single model output aggregated over India
Nayak et al. (2015)	–	1981–2006	*−0.01*[c]	Aggregated over India
Top-down				
Thompson et al. (2016)	IS	1996–2012	*−0.05 (−0.18 to 0.03)*	Ensemble of models
Patra et al. (2011)	IS + CARIBIC	2007–2008	−0.37 ± 0.20	Single model output
Niwa et al. (2012)	IS + CONTRAIL	2006–2008	*−0.13*	Single model output
Jiang et al. (2014)	IS + CONTRAIL	2006–2008	*−0.11 ± 0.30*	Single model output
Swathi et al. (2021)	IS + regional flask data[d]	2006–2011	*−0.27 to −0.08*	Single model output aggregated over India
OCO-2 v9 MIP[e]	IS	2015–2018	*−0.07 ± 0.68*	Ensemble of models
OCO-2 v9 MIP	OCO-2 LN + LG	2015–2018	*−0.08 ± 0.54*	Ensemble of models
This Study	IS	2015–2018	0.04 ± 0.14	Single model output
This study	OCO-2 LN + LG	2015–2018	0.04 ± 0.14	Single model output

[a]See respective publications for more details about definitions and individual components considered while calculating CO_2 flux budgets shown here, and the specifics about the South Asia region boundaries. Special note is added in the fifth column whenever CO_2 flux budget values represent India instead of entire South Asia region. [b]Value represents bottom-up net land-atmosphere carbon estimate over south Asia including lateral carbon fluxes (see details in Ciais et al., 2020). [c]Value denotes long-term NEE flux over India. [d]The flask data from three stations (HLE, PON, and PBL) and hourly continuous data at HLE over South Asia were assimilated along with global IS data. [e]Values taken from OCO-2 v9 MIP website.

4.2. Annual NBE Over South Asia

Table 2 shows the multi-year mean South Asian carbon budget of the prior and posterior CO_2 fluxes. The posterior multi-year mean annual NBE over South Asia is near neutral (0.04 ± 14 PgC yr^{-1}), both when assimilating IS observations or OCO-2 LN + LG observations. The multi-year mean posterior estimates for both the IS and OCO-2 assimilations (0.04 PgC yr^{-1}) are close to the prior (−0.01 PgC yr^{-1}); however, the interannual variability is higher (see Figure 2). *SD* values are larger in the IS and OCO-2 posteriors (0.14 PgC yr^{-1}) compared to the prior (0.03 PgC yr^{-1}) as shown in Table 2. The OCO-2 v9 MIP estimated South Asian NBE of −0.07 ± 0.68 PgC yr^{-1} with IS observations and −0.08 ± 0.54 PgC yr^{-1} with LN + LG observations (Table 2). Past studies using global inverse models and bottom-up ecosystem models have predicted an annual mean flux for the South Asia region ranging from −0.37 to −0.05 PgC yr^{-1} (Cervarich et al., 2016; Ciais et al., 2020; Jiang et al., 2014; Niwa et al., 2012; Patra et al., 2011, 2013; Thompson et al., 2016) for different time periods (years up to 2013; see Table 3). The mean annual flux estimated for the South Asia region in this study (2015–2018) is slightly higher than this range (consistent when considering *SD* values), likely due to the larger positive NBE anomalies in 2016–2017 following the 2014–2016 El Niño event (see Figure 2). Direct comparison of regional-scale top-down and bottom-up CO_2 flux estimates should in fact consider lateral carbon flux sources such as crop trade and riverine export (Ciais et al., 2020; Kondo et al., 2020) as noted by Ciais et al. (2021). Overall, the multi-year mean annual NBE estimates in this study are comparable with estimates from the OCO-2 v9 MIP and previous studies focused on South Asia.

Annual mean and multi-year mean NBE (and anomalies) over South Asia are shown in Figure 2. The IS-constrained annual mean NBE shows a CO_2 source for 2015 (0.22 PgC yr^{-1}) and sink for 2016 (−0.12 PgC yr^{-1}). This differs from the OCO-2-constrained estimates which resulted in a CO_2 sink for 2015 (−0.14 PgC yr^{-1}) and source for 2016 (0.14 PgC yr^{-1}). Figure 2 reveals contrasting posterior annual NBE anomaly values using IS (positive NBE anomaly of 0.19 PgC yr^{-1} for 2015) versus OCO-2 LN + LG (positive NBE anomaly of ∼0.11 PgC yr^{-1} for 2016–2017) observation modes. IS- and OCO-2-constrained NBE for the region were more comparable for 2018 with both simulating near-neutral biospheres. The absence of IS observations over the South Asia region might

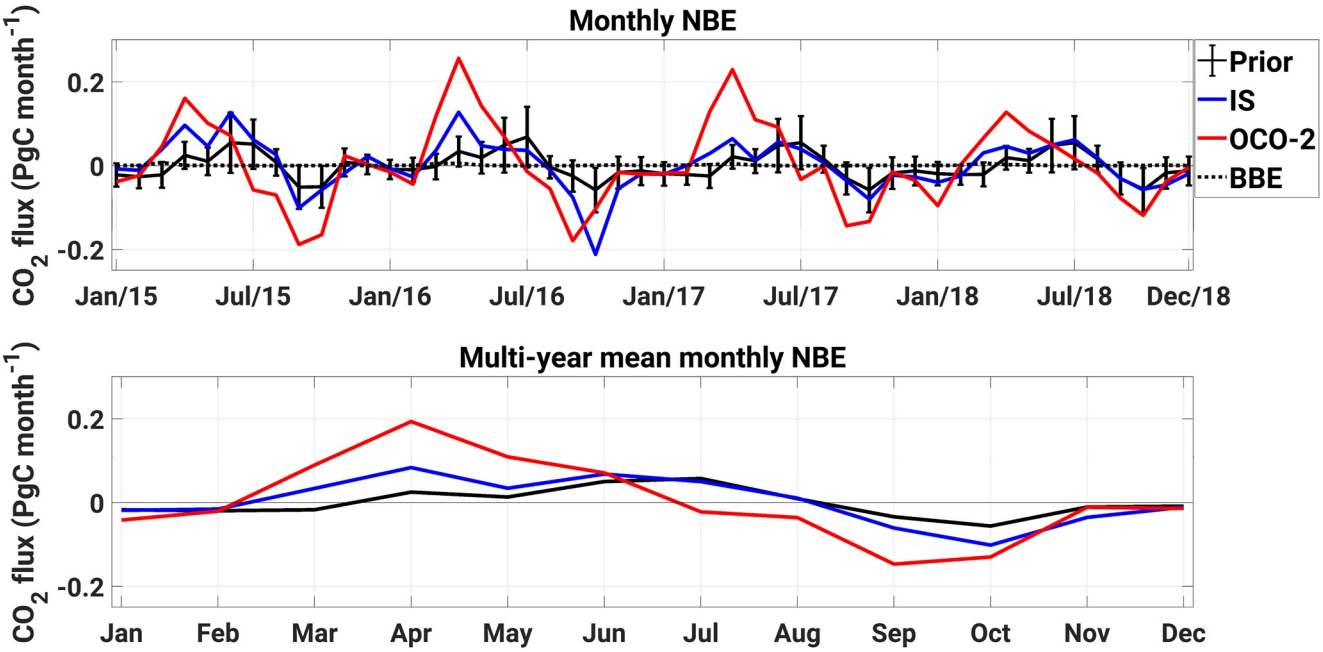

Figure 3. Monthly NBE (PgC month^{-1}, top panel) and multi-year mean monthly NBE (PgC month^{-1}, bottom panel) over South Asia from the prior model (solid black line), and posteriors optimized with IS (blue) and OCO-2 LN + LG (red) observations. In the top panel, error bars on the prior fluxes represent prior flux uncertainty assumed during the assimilation. The dashed black line in the top panel depicts unoptimized BBE.

have resulted in some of the contrasting features (for years 2015–2016) compared to OCO-2. The positive anomaly for 2016–2017 predicted using the OCO-2 LN + LG observations (likely due to the impact of 2014–2016 El Niño event), which was not captured when assimilating IS data, illustrates the differences in CO_2 flux estimates due to varying observational coverage of the two data sources.

4.3. Monthly NBE Over South Asia

Here, we examine the constraints imposed by OCO-2 XCO_2 data to the seasonal cycle of terrestrial biospheric fluxes over South Asia. Figure 3 shows monthly mean NBE fluxes over South Asia from 2015 to 2018 optimized by IS and OCO-2 LN + LG observation modes. It is clear from the figure that the unconstrained biomass burning CO_2 emission is minor compared to NEE fluxes, suggesting that BBE is not a significant carbon source over South Asia. The most striking feature of the monthly NBE fluxes optimized with OCO-2 data is the stronger seasonal amplitude compared to fluxes optimized with IS data and prior fluxes used in the inversions. The IS-constrained fluxes also show a larger seasonality compared to prior CASA model fluxes, although the amplitude is not as strong as OCO-2 based inversion. OCO-2 optimized NBE seasonal amplitude is largest for years 2016 (0.44 PgC month^{-1}) and lowest for year 2018 (0.32 PgC month^{-1}). Figure 3 also shows multi-year mean monthly NBE fluxes for the South Asia region. The prior and IS-constrained NBE show a seasonal amplitude of 0.11 and 0.19 PgC month^{-1}, respectively, whereas OCO-2 resulted in larger seasonal amplitude of 0.34 PgC month^{-1}. The magnitude of the NEE seasonality estimated by assimilating OCO-2 data is noticeably larger than our current understanding of NEE in this region (represented by the prior NEE used in the model, and ensemble mean NEE from the Multiscale Synthesis and Terrestrial Model Intercomparison Project (MsTMIP; Fisher, Sikka, Huntzinger, Schwalm, & Liu, 2016, Fisher, Sikka, Huntzinger, Schwalm, Liu, Wei, et al., 2016; Huntzinger et al., 2013, 2018) with a seasonal amplitude of 0.16 PgC month^{-1}; see top panel of Figure 4).

The OCO-2 v9 MIP ensemble mean estimate also depicts similar seasonality with the OCO-2 and IS data assimilations calculated in our model (see the OCO-2 v9 MIP ensemble mean and individual models in Figure S2 in Supporting Information S1). It has been shown that differences in vertical transport simulated by the two main CTMs used in the OCO-2 v9 MIP (i.e., GEOS-Chem and TM5) can lead to variability in regional optimized CO_2 flux estimates (Schuh et al., 2019). However, the seasonal distribution and amplitude of NEE in South Asia presented in this study is consistent with the majority of ensemble members in the OCO-2 v9 MIP including

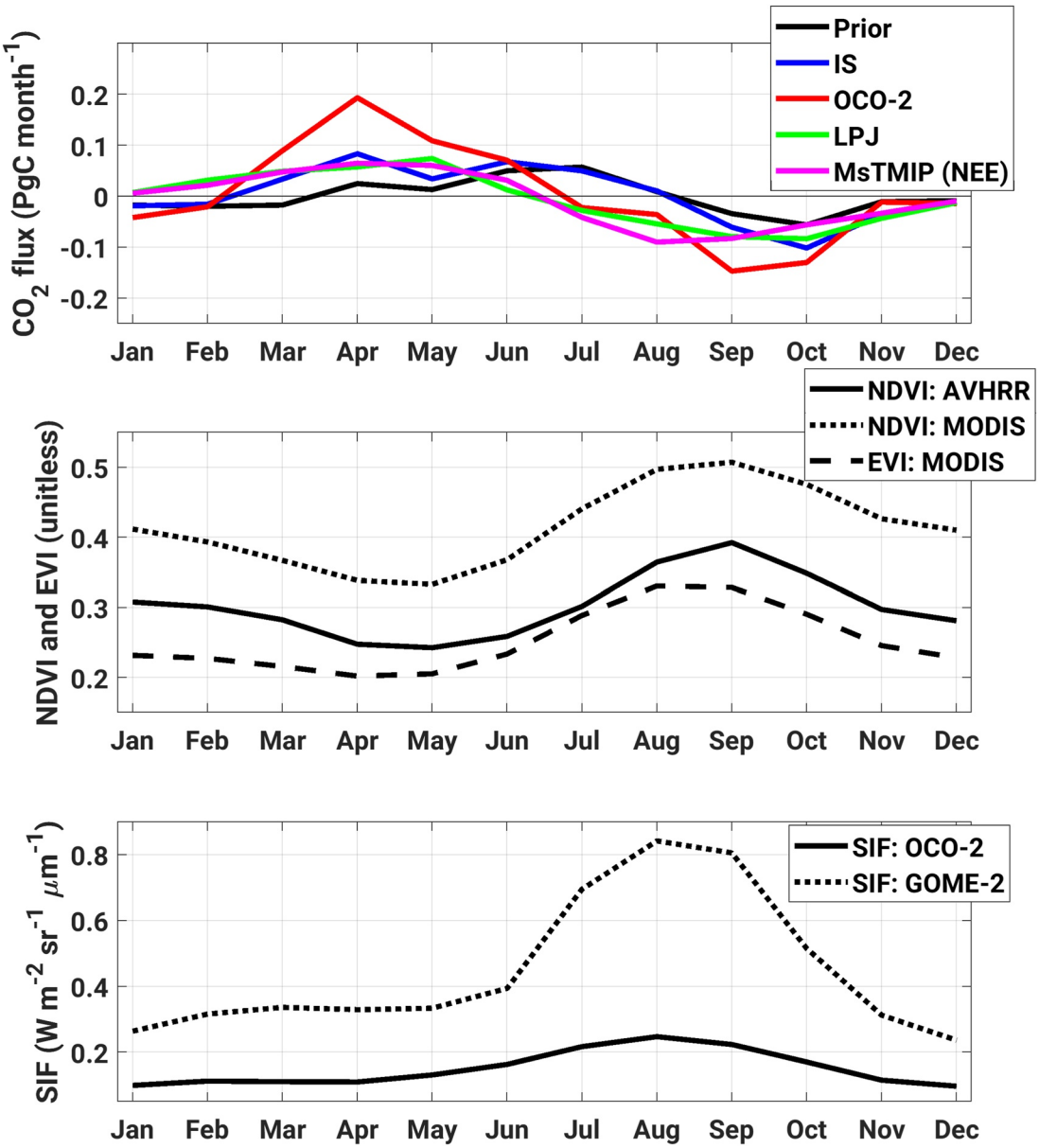

Figure 4. Comparison of South Asian multi-year mean monthly NBE (PgC month^{-1}) from the prior model (CASA; solid black line), posteriors optimized with IS (blue) and OCO-2 LN + LG (red) observations, NBE from the LPJ model (green), and the MsTMIP ensemble mean NEE ("optimal" or "weighted" ensemble mean from 15 global land surface models; magenta; top row). These values are further compared with NDVI (unitless) from the AVHRR and MODIS, EVI (unitless) from MODIS (middle row), and SIF (W m^{-2} sr^{-1} μm^{-1}) from the GOME-2 and OCO-2 (bottom row).

predictions from both GEOS-Chem and TM5 models (Figure S2 in Supporting Information S1). Figure S2c in Supporting Information S1 shows that six out of nine inverse models predict posterior CO_2 flux estimates constrained by OCO-2 LN + LG data have larger seasonality than the assumed priors. Furthermore, this figure shows that seven out of nine ensemble members of the v9 OCO-2 MIP had similar phase shifts in South Asian NEE seasonality presented in the results of this study.

Another noticeable feature imposed by OCO-2 XCO_2 data was the phase shift of the seasonal cycle compared to the prior NEE model. OCO-2 data leads to the prediction of a shift in peak CO_2 source and sink 1–3 months earlier than those predicted by the CASA prior model. OCO-2 optimized NBE shows CO_2 release from the biosphere from March to May (pre-monsoon season), with a pronounced peak source around April, whereas CASA has a broad peak between April and July (pre-monsoon to summer monsoon season) months. The OCO-2 observations

Table 4
Comparison of the Key Features of South Asian NEE Seasonal Cycle Obtained in This Study With Previous Studies

Study	Details of the study				NEE Seasonal amplitude (PgC month^{-1})[a]			Months with peak CO_2 source[b]			Months with peak CO_2 uptake[b]		
	TransportModel	Prior model	Years simulated	Regional data used	Prior	IS[c]	Regional data or OCO-2[d]	Prior	IS	Regional data or OCO-2[d]	Prior	IS	Regional data or OCO-2[d]
This Study	GEOS-Chem	CASA	2015–2018	OCO-2	0.11	0.18	0.33	April–July	April	April	October	October	September
Patra et al. (2011)	ACTM[e]	CASA	2008	CARIBIC	0.13	0.13	0.25	April–July	April–July	April	October	August–September	August–September
Niwa et al. (2012)	NICAM-TM[f]	CASA	2006–2008	CONTRAIL	0.13	0.13	0.29	April–July	April–June	June[g]	October	October	August–September
Jiang et al. (2014)	TM5[h]	BEPS[i]	2006–2008	CONTRAIL	0.17	0.29	0.29	April–May	April–May	April–June	August–October	September	September

[a]The seasonal NEE amplitude values for other studies are approximate values inferred from figures in those studies (Patra et al., 2011 [Figure 3], Niwa et al., 2012 [Figure 5], and Jiang et al., 2014 [Figure 7]). [b]Months with peak NEE source and uptake are assessed by visual inspection of figures in those studies. A range of months (e.g., April–July) are provided here when a distinct peak could not be identified by visual inspection of the figures. [c]IS refers to the ObsPack data (for this study) or the GLOBALVIEW-surface CO_2 data (for other studies) assimilated in the inversions. [d]For three previous studies, data in this column is corresponding to joint inversion assimilating the GLOBALVIEW-surface CO_2 data and regional passenger aircraft data. For the present study, data in this column is corresponding to the inversion assimilating OCO-2 LN + LG data. [e]ACTM = Atmospheric general circulation model-based Chemistry Transport Model. [f]NICAM-TM = Nonhydrostatic Icosahedral Atmospheric Model-based Transport Model. [g]Large CO_2 source for April–June with a distinct peak during June. [h]TM5 = Transport Model-5. [i]BEPS = Boreal Ecosystems Productivity Simulator.

lead to the largest CO_2 uptake at the end of the summer monsoon (September) rather than October (start of post-monsoon season) as predicted by the prior CASA model. The prediction of the phase shift in seasonal NBE in our model agrees with seven out of nine models in the OCO-2 v9 MIP which also predicted peak positive NEE in April, and negative NEE in September (see Figure S2 in Supporting Information S1).

Figure 4 (top panel) shows that the MsTMIP model ensemble mean, which represents our current understanding of bottom-up "climatological" CO_2 fluxes over this region, has a peak source distributed between March and June, and peak drawdown between August and September. While biomass burning fluxes of CO_2 are small for the South Asia region, the emission of CO_2 from fires has a peak in March–April (Patra et al., 2013) and could contribute slightly to the flux seasonality predicted when assimilating observations. The seasonal agriculture crop residue burning source (Jethva et al., 2019) is part of the CASA-GFED-4.1s prior BBE source applied in this study (van der Werf et al., 2017), and does not contributing significantly to the seasonal magnitudes (see total BBE source in Figure 3). However, residential biofuel usage is recognized as a significant source of carbonaceous aerosols in this region; however, not as a large contributor to CO_2 (Venkataraman et al., 2005). Limited literature is available describing the seasonal variability of biofuel source components in the South Asia region. Since residential biofuel emissions are not considered in our prior emissions, its contribution could be part of the posterior NEE seasonal magnitude estimated in this study. The CASA-GFED3 inventory (van der Werf et al., 2010) as applied in Philip et al. (2019) indicates that biofuel emissions of CO_2 in South Asia are a relatively small source (~0.05 PgC yr^{-1} in 2015 which is <10% of fossil fuel emissions and ~5 times that of BBE emissions used as a prior in this study over South Asia), and is likely not the primary contributor to the NEE seasonal cycle of amplitude derived here. Apart from these minor contributions from biofuel sources and potentially un-accounted biomass burning components, the seasonality in NBE as described in this section is considered to be primarily due to terrestrial biosphere processes such as photosynthesis and respiration. Note that the seasonal variability of terrestrial biosphere is driven by several interrelated variables, such as temperature, solar insolation, rainfall (e.g., Braswell et al., 1997). We compare NBE estimates in this study with multiple satellite-derived vegetative indices in Section 4.5.

Table 4 shows the comparison of NEE seasonality estimated in this study (note that we report NEE instead of NBE to be consistent with three previous studies) against three previous studies assimilating regional aircraft CO_2 measurements (CARIBIC and CONTRAIL) in addition to GLOBALVIEW global surface data (Jiang et al., 2014; Niwa et al., 2012; Patra et al., 2011). The prior, IS-constrained, and OCO-2-constrained NEE (NBE) show a seasonal amplitude of 0.11 (0.11), 0.18 (0.19), and 0.33 (0.34) PgC month^{-1}, respectively. Table 4 shows that the past three studies displayed differences among them in estimating the seasonal amplitude, and the timing of peak CO_2 source and sink months. However, all three studies found a strong seasonal NEE amplitude of ~0.25–0.29 PgC month^{-1} when assimilating regional aircraft CO_2 measurements in addition to GLOBALVIEW global surface data (joint inversion using surface-based and aircraft-based data). These three previous studies based on different transport models, prior biosphere models and passenger aircraft datasets (see details in Table 4) found that the inclusion of regional aircraft data into the assimilation system resulted in larger NEE seasonal amplitude (~0.25–0.29 PgC month^{-1}), comparable to estimates in this study (0.33 PgC month^{-1}). All three past studies constrained with regional aircraft data predicted largest

Table 5
Statistics From the Comparison of Model Simulated Prior and Posterior Atmospheric CO_2 Concentrations and XCO_2 Against Global Observations

	Global ObsPack CO_2[a]				OCO-2 LN and LG XCO_2			
	NMB (ppm)	SDE (ppm)	RMSE (ppm)	*R*	NMB (ppm)	SDE (ppm)	RMSE (ppm)	*R*
	N[b] = 24,898 (773,042)[a]				*N* = 334,697			
Prior	1.39 (1.17)[a]	4.95 (4.72)	5.50 (5.15)	0.82 (0.81)	1.68	1.47	2.10	0.93
IS	−0.03 (−0.06)	3.81 (3.47)	3.81 (3.48)	0.88 (0.88)	0.11	1.25	1.25	0.94
OCO-2	−0.48 (−0.45)	4.40 (4.21)	4.46 (4.26)	0.84 (0.83)	−0.06	0.97	0.97	0.96

[a]Statistical values and *N* outside parentheses correspond to "withheld" data, while values within the paratheses correspond to "assimilated" data. [b]*N* is the total number of observations for 2015–2018 used to calculate the statistical parameters in the table.

CO_2 sources around April (ranges from April to June) which is generally consistent with OCO-2 optimized NEE in this study (although OCO-2 resulted in a more pronounced peak source in April). The shift of peak CO_2 uptake from October (as in CASA prior model) to September is generally consistent with all the three past studies. In short, the assimilation of column CO_2 observations from the OCO-2 satellite over South Asia indeed added robust constraints on regional flux estimates, leading to higher terrestrial biospheric CO_2 flux seasonal amplitudes and a phase shift in seasonal cycle, as found by previous studies assimilating South Asian aircraft-based in situ observations. This suggests that OCO-2 data imposes constraints on regional NEE fluxes in a similar manner as regional in situ aircraft data and can effectively be used to investigate biospheric carbon processes at spatial scales smaller than TransCom-3 regions.

The stronger seasonal cycle imposed by satellite data for the Northern Tropical latitudinal band regions (0°–23°N; comprising the northern parts of the South Asia region considered in this study) was documented by earlier studies based on GOSAT satellite retrievals (Palmer et al., 2019) and version 7 of OCO-2 (Crowell et al., 2019). The strong seasonal cycle amplitude of NEE fluxes over a region proximal to South Asia (Tropical Asia region: TransCom-3 region 9) was reported by Basu et al. (2014) based on GOSAT data assimilations. Consistent with these past studies, this work found strong CO_2 flux seasonality over South Asia. Since these regions (Northern Tropics, South Asia, and Tropical Asia) have distinct terrestrial biosphere features (e.g., croplands, tropical forests), different natural and/or land-use processes might be causing the larger seasonality over these regions. The comparison of OCO-2 optimized fluxes over South Asia with previous studies assimilating regional aircraft data (Jiang et al., 2014; Niwa et al., 2012; Patra et al., 2011) reveals that the seasonality and phase shift in monthly NBE flux is likely to be realistic.

We conducted several additional sensitivity model simulations to emphasize that the South Asian CO_2 flux seasonality results presented in this study are robust and not dependent on the assumed prior model, prior mean NEE magnitude/seasonality, or prior error values applied (see Text S1 and Figure S3 in Supporting Information S1 for details of these sensitivity model simulations).

4.4. Evaluation of Optimized CO_2 Fields

Table 5 summarizes the evaluation statistics of model simulated atmospheric CO_2 concentrations and XCO_2 values, using the prior and posterior CO_2 fluxes against observations across the globe. The simulated CO_2 mole fractions and XCO_2 values using prior fluxes show a consistent positive global bias compared to withheld and assimilated ObsPack (1.39 and 1.17 ppm, respectively), and OCO-2 data (1.68 ppm), suggesting an overestimated prior flux used in the inverse model. All posterior CO_2 and XCO_2 values assimilating IS and OCO-2 LN + LG data show substantial reductions in NMB and SDE, and corresponding increases in correlation, as compared to prior values. A negative bias of −0.03 to −0.48 ppm with SDE values of 3.81–4.40 ppm were obtained while comparing IS and OCO-2-constrained CO_2 concentrations against withheld ObsPack observations. The comparison against both withheld and assimilated ObsPack data leads to similar model performance statistics. The OCO-2-constrained XCO_2 simulated values perform better than IS-constrained XCO_2 when compared against assimilated OCO-2 LN and LG data (RMSE of 0.97 ppm for OCO-2 vs. 1.25 ppm for IS). In contrast, when compared with

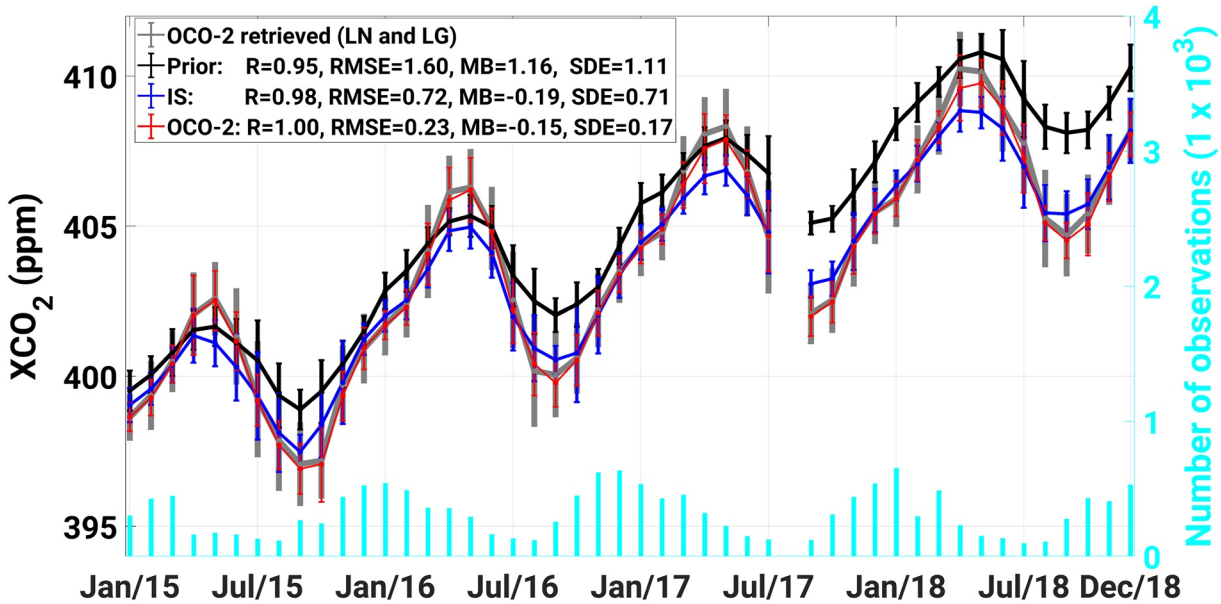

Figure 5. Comparison of monthly averaged OCO-2 retrieved LN and LG XCO_2 (ppm) over South Asia (region boundaries in Figure 1), and the values simulated from the prior model (black line) and those optimized with in situ (IS, blue line), and OCO-2 (LN + LG assimilation, red line) observations. Error bars represent the standard deviation of the mean monthly values. The legend contains evaluation statistics of monthly mean values during 2015–2018. The cyan bars represent the total number of OCO-2 retrieved LN and LG observations per month. The failure of the OCO-2 sensor during August and early September 2017 led to a gap in the monthly time series data.

withheld or assimilated ObsPack data, the IS-constrained CO_2 concentrations (RMSE of 3.81–3.48 ppm) perform better than OCO-2-constrained fields (RMSE of 4.46–4.26 ppm). The overall model performance against ObsPack and OCO-2 data was comparable to other global models which participated in the OCO-2 v9 MIP).

Figure 5 shows the comparison of OCO-2 retrieved XCO_2 versus model-estimated prior and posterior XCO_2 averaged over the South Asia region. The seasonal cycle of OCO-2 retrieved XCO_2 is larger than simulated XCO_2 using prior fluxes in the forward model. The posterior XCO_2 estimated when assimilating either IS or OCO-2 LN + LG observations agree better with OCO-2 retrieved data, compared to prior model simulated XCO_2 values. As expected, the LN + LG based posterior XCO_2 values had better agreement with OCO-2 retrieved XCO_2 compared to IS-based posterior predictions. Figure 5 also shows a noticeable seasonality in the number observations over South Asia, with lower number of observations during the summer monsoon season (June-September) due to cloud cover obscuring the satellite field of view. We recognize that the temporal variability in observation coverage could lead to uncertainties in the optimized flux estimates over South Asia (Byrne et al., 2017; Liu et al., 2014). However, since the posterior XCO_2 values predicted when assimilating OCO-2 LN + LG observations agree well with satellite data (that is, assimilated OCO-2 LN + LG data) during all seasons, this suggests that OCO-2 observations are sufficient enough to predict robust NEE fluxes throughout the annual cycle.

Figure 6 shows the comparison of model simulated CO_2 concentrations against monthly averaged aircraft-based data from the CONTRAIL project (Machida et al., 2008) near and downwind of the South Asia region. Since CONTRAIL observations over the South Asia region are not available during the time period considered in this study (except for a single flight track near Sri Lanka in 2015; see CONTRAIL website), we used free and upper tropospheric observations averaged over the latitude bands containing the South Asia region (latitude band between 4°N and 32°N, longitude band between 57.5°E and 132.5°E, altitude range of ~5 to 13 km). The unassimilated CONTRAIL data for 2015–2016 available publicly as part of the ObsPack data package (see Section 2.1.2) is used here. The seasonality of CONTRAIL CO_2 mixing ratios show highest values during May and lowest values during September. It is noteworthy that OCO-2 LN and LG XCO_2 retrievals averaged over the South Asia region in Figure 5 show similar seasonality. The similarity in OCO-2 XCO_2 retrievals versus CONTRAIL aircraft measurements could be due to the fact that deep convection in this tropical region leads to upper tropospheric CO_2 being influenced by surface CO_2 fluxes. Umezawa et al. (2018) found that the upper tropospheric minimum in the Northern Tropical latitudes during August–September months is due to large uptake of CO_2 by the South

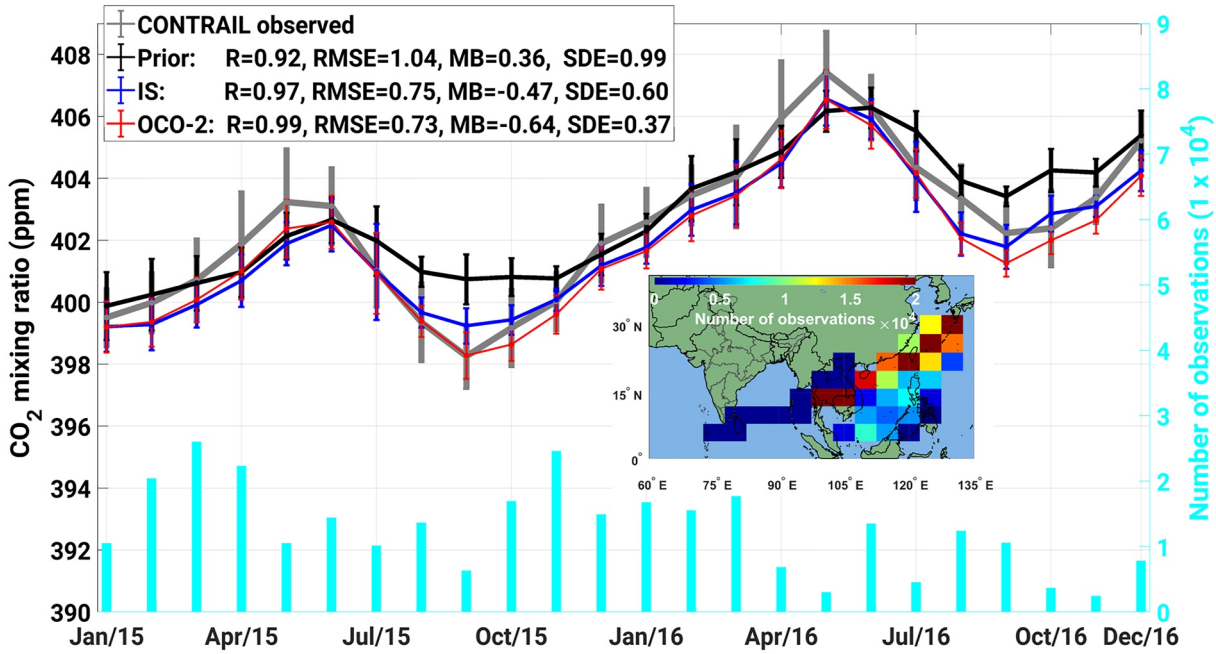

Figure 6. Comparison of monthly averaged CONTRAIL observed CO_2 mixing ratio (ppm) at the altitude range of ~5 to 13 km near and downwind of the South Asia region (see map in the inset) and the values simulated from the prior model and those optimized with in situ (IS) and OCO-2 (LN + LG assimilation) observations. Error bars represent the standard deviation of mean monthly values. The legend contains evaluation statistics of monthly mean values during 2015–2016 and the inset shows the total number of CONTRAIL observations per grid cell. The cyan bars represent total number of CONTRAIL observations per month.

Asian terrestrial biosphere. The seasonal pattern of CONTRAIL observations was reproduced by posterior CO_2 constrained by both IS and OCO-2 data (R = 0.97–0.99) much better than the prior (R = 0.92) by correcting the high bias of prior model during July–October (Figure 6).

Figure 7 shows the comparison of model simulated CO_2 concentrations against surface flask measurements from four monitoring stations over South Asia. The representativeness of these four stations has already been studied in detail in previous studies and found that these stations are influenced by local sources and sinks, long-range transport, and monsoon circulation (Lin et al., 2015; Nalini et al., 2018; Tiwari et al., 2014; Tiwari, Valsala, Vellore, & Kunchala, 2013). Overall, the performance of model simulations in this study against surface flask data from these four stations is less accurate compared to the performance against global observations described above. The poor performance over these sites could be due to representativeness issues arising from the proximity of local emissions and regional biosphere sources to these monitoring stations (Lin et al., 2015, 2018; Tiwari et al., 2014; Tiwari, Revadekar, & Ravi Kumar, 2013; Tiwari, Valsala, Vellore, & Kunchala, 2013), difficulties simulating transport over complex terrains (e.g., mountain sites), and the coarse resolution of the GEOS-Chem model not capturing land/ocean dynamics and complex topography. Note that a previous study (Lin et al., 2018) found poor correlation (R < 0.3) in the synoptic variability of CO_2 concentrations simulated with a high-spatial-resolution (~0.51° × ~0.66°) nested regional model compared against flask observations from all four stations considered here. Lin et al. (2018) also found that the seasonal amplitude of model-simulated CO_2 concentrations was underestimated by ~30% to 50% when compared against flask data from the SNG, PON, HLE, and PBL stations. Another study by Nalini et al. (2018) found >15 ppm differences in the comparison of GOSAT and CarbonTracker-based model estimates against flask measurements from SNG and another station in India which ceased operation in 2012.

Despite the large MB and SDE, Figure 7 shows that the assimilation of OCO-2 LN + LG data leads to some improvements in the temporal correlation and slight reductions in SDE compared to prior and IS-based inversions (except at the PON station). In particular, OCO-2 data assimilation resulted in the model better capturing the temporal variability and seasonality of observations compared to prior and IS data over the HLE station (location is characterized by clean background air masses (Lin et al., 2015)). The fact that HLE station is not primarily influenced by local sources and sinks, and measures regional free tropospheric air is likely the reason why our

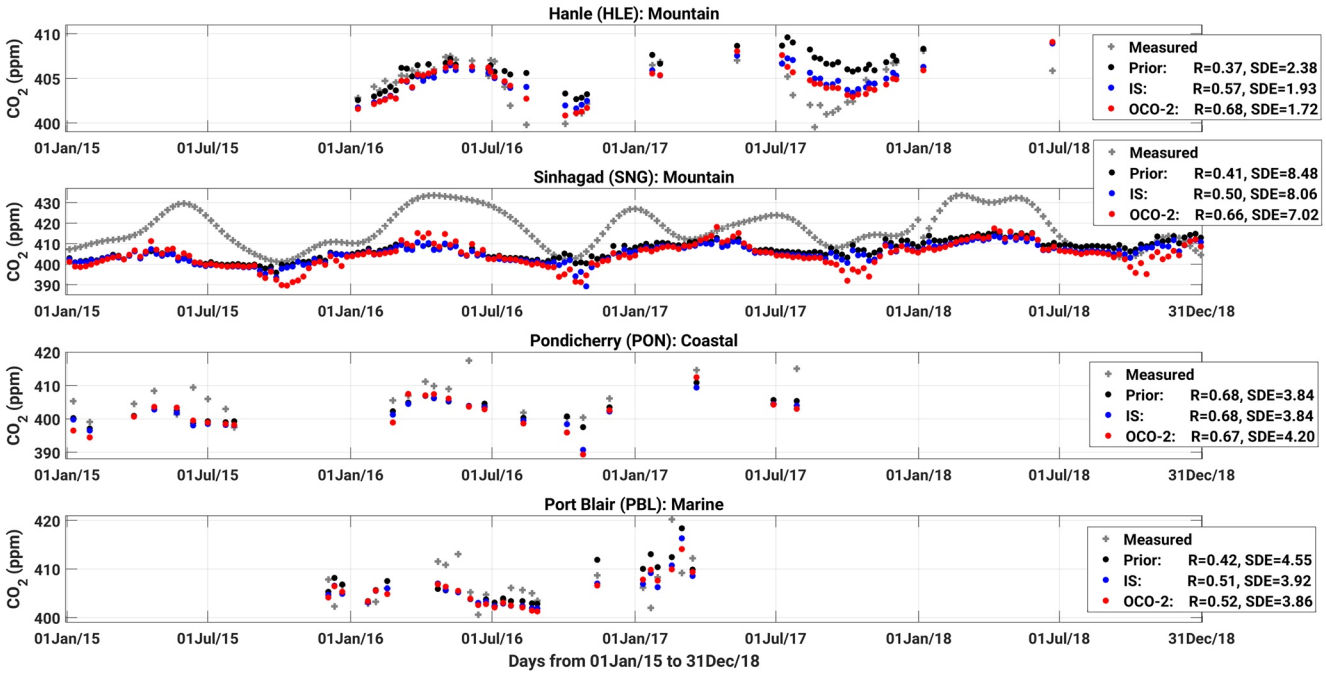

Figure 7. Time series of CO_2 flask measurement data (ppm; gray crosses) from four South Asian monitoring stations, and co-sampled CO_2 concentrations from the prior model (black dots) and model-predictions optimized with IS (blue dots) and OCO-2 LN + LG (red dots) data.

model simulations compare most favorably to HLE observations in comparison to the other three stations. Note that Swathi et al. (2021) also found a smaller posterior model-data mismatch (<2 ppm) at the HLE site compared with PON and PBL sites, while assimilating HLE, PON, and PBL flask data along with global IS data in a global inverse system at 2.5° × 3.75° spatial resolution (Chevallier et al., 2010). Over the SNG station, there is large seasonal amplitude over SNG site (>30 ppm) which most models (Lin et al., 2018; Nalini et al., 2018) fail to represent; however, the OCO-2 constrained posterior improves the temporal correlation (R = 0.66) compared to prior (R = 0.41) and IS (R = 0.50) constrained posteriors. Considering the limited evaluation conducted here against flask data from four stations (Figure 7), CONTRAIL data near the South Asia region (Figure 6) and OCO-2 XCO_2 observations (Figure 5), we conclude that OCO-2 data better constrains the seasonality of CO_2 mixing ratios over South Asia compared to prior and IS. A robust evaluation cannot be conducted here due to lack of continuous observations over the region (although we acknowledge that there could be other short-term measurements over select locations; e.g., Sreenivas et al., 2019) other than the four flask monitoring stations considered in this study.

4.5. NBE Flux Seasonality Compared With Vegetation Indices

Figure 4 shows the comparison of South Asian prior and optimized monthly NBE against vegetation indices. Table 6 shows the temporal correlation of NBE and the vegetation indices. The negative correlation of NDVI, EVI, and SIF data against NBE data were expected, since these satellite-retrieved variables are highly correlated with estimates of gross primary productivity (GPP). Most importantly, this study reveals a much higher correlation (negative) of NDVI (AVHRR and MODIS) and EVI versus OCO-2 constrained NBE (R = −0.73 to −0.85), compared to IS-constrained NBE (R = −0.41 to −0.59). The CASA prior and IS-constrained NEE are poorly correlated with SIF data (R < −0.14); however, the comparison of both GOME-2 and OCO-2 derived SIF data against OCO-2 optimized NEE reveals a moderate to strong negative correlation (R = −0.47 to −0.49). SIF retrievals from satellites capture the photosynthetic activity of the terrestrial biosphere

Table 6
Correlation Coefficients Between Multi-Year Monthly Mean Vegetative Indices (NDVI, EVI, and SIF) and NBE From the Prior and Posterior (Using IS and OCO-2 LN + LG Observations) and the LPJ Biosphere Model

NBE	NDVI (AVHRR)	NDVI (MODIS)	EVI (MODIS)	SIF (GOME-2)	SIF (OCO-2)
Prior	−0.53	−0.40	−0.18	0.07	0.18
IS	−0.71	−0.68	−0.47	−0.16	−0.10
OCO-2	−0.87	−0.89	−0.77	−0.50	−0.47
LPJ	−0.85	−0.95	−0.87	−0.64	−0.63

(Frankenberg et al., 2016) and have been found to help constrain regional-scale NEE spatiotemporal variability (Shiga et al., 2018; Sun et al., 2017) and could be a better proxy of photosynthesis than EVI (Luus et al., 2017). In general, the OCO-2 constrained NBE are better correlated with satellite-based NDVI, EVI, and SIF data compared to prior and IS-constrained model simulations. Since we used a diagnostic model as a prior in inverse model simulations, we also compare NBE from a fully prognostic meteorologically driven biosphere model (LPJ; Poulter et al., 2014) to the same set of vegetation indices. Even though the LPJ model was not driven with vegetative index data, LPJ NBE shows large negative correlation with all satellite-based variables, such as NDVI, EVI, and SIF. Overall, from the strong temporal correlation of OCO-2 optimized NBE against satellite-based NDVI, EVI, and SIF data, the better agreement of OCO-2 optimized CO_2 mole fraction and XCO_2 data against independent measurements (Section 4.4), and the consistency of OCO-2 optimized flux seasonality compared with past studies assimilating regional observations (Section 4.3), we conclude that the seasonal variability of the OCO-2 constrained NBE in South Asia is robust.

5. Conclusions

We examined the annual, interannual, and seasonal cycle of terrestrial biospheric CO_2 fluxes over South Asia region by assimilating OCO-2 satellite CO_2 column retrievals in a global top-down inversion model. We conducted global inverse model simulations using the OCO-2 version 9 retrievals and global IS observations, and analyzed posterior NBE aggregated over South Asia from 2015 to 2018. The flux inversion system was evaluated by comparing the optimized atmospheric CO_2 concentration fields against global and regional observations.

This study determined that between 2015 and 2018, the South Asian terrestrial biosphere is near-neutral, with a multi-year mean annual NBE of 0.04 ± 0.14 PgC yr^{-1} estimated from both IS or OCO-2 (LN + LG) observations. We find contrasting posterior annual NBE anomaly values using IS (positive NBE anomaly of 0.19 PgC yr^{-1} for 2015) versus OCO-2 (positive NBE anomaly of ~0.11 PgC yr^{-1} for 2016–2017) observations. The most striking result found from assimilating OCO-2 observations was the constraint imposed on the seasonal cycle of NBE fluxes. The seasonality of South Asian NEE estimated by assimilating OCO-2 data showed a larger seasonal cycle compared to the current understanding of NEE in this region (represented by the prior NEE used in the model and MsTMIP ensemble mean NEE). The OCO-2 LN + LG inversion led to NBE seasonal amplitude of 0.34 PgC $month^{-1}$, compared to 0.19 PgC $month^{-1}$ in the IS-based inversion, 0.11 PgC $month^{-1}$ in the prior model, and 0.16 PgC $month^{-1}$ in the MsTMIP ensemble mean NEE product. Three previous studies (Jiang et al., 2014; Niwa et al., 2012; Patra et al., 2011), assimilating regional aircraft CO_2 measurements in addition to global surface data, also found larger seasonal amplitudes for the South Asian region (0.25–0.29 PgC $month^{-1}$). We find that OCO-2 data also imposed a phase shift in the seasonal cycle, resulting in the largest CO_2 source occurring in April and a largest uptake in September. The NBE peak source/sink months in April/September are generally consistent with regional IS data assimilation model studies (Jiang et al., 2014; Niwa et al., 2012; Patra et al., 2011). The seasonality of OCO-2 optimized NBE had better correlation with satellite-retrieved vegetation indices (NDVI, EVI, and SIF data) than the prior and IS constrained NBE estimates. This study therefore suggests that the seasonality imposed by OCO-2 data over South Asia is robust, and OCO-2 satellite can be effectively used to optimize biospheric carbon processes on a sub-regional scale in a similar manner as regional aircraft in situ data networks.

To our understanding, this is the first study analyzing OCO-2 constrained terrestrial biospheric CO_2 fluxes over a small region/sub-continent, at smaller spatial scales compared to TransCom-3 regions, or latitude bands as assessed by previous studies. A robust evaluation of the inversion system used in this research, and its inferred fluxes, cannot be conducted over South Asia due to lack of continuous observations. Therefore, the findings from this article should be examined in future studies assimilating in situ and vertically resolved observations along with satellite data in a regional inverse modeling system. The expansion of observational networks over South Asia in recent years (e.g., Lin et al., 2015; Nalini et al., 2019; Tiwari et al., 2014) could help such regional inverse modeling efforts.

Conflict of Interest

The authors declare no conflicts of interest relevant to this study.

Data Availability Statement

The forward and inverse model simulations for this work were performed using the GEOS-Chem model, which is publicly available at http://wiki.seas.harvard.edu/geos-chem/index.php/GEOS-Chem_Adjoint. The CarbonTracker CT2019 fluxes used as prior information in the model simulations can be accessed from the website http://carbontracker.noaa.gov. The CarbonTracker CT2019 documentation is available at https://www.esrl.noaa.gov/gmd/ccgg/carbontracker/CT2019_doc.php. For this study, we used OCO-2 10-s average XCO_2 data and corresponding error estimates from ftp.cira.colostate.edu:/ftp/BAKER/OCO2_b91_10sec_GOOD_r24.nc4. The OCO-2 individual sounding data can be downloaded from https://oco.jpl.nasa.gov. We used the ObsPack data packaged for the OCO-2 v9 MIP (https://www.esrl.noaa.gov/gmd/ccgg/obspack/data.php?id=obspack_co2_1_OCO2MIP_v2.1_2019-08-15). The protocol of the OCO-2 v9 MIP, details of input data, and validation statistics can be accessed from https://www.esrl.noaa.gov/gmd/ccgg/OCO2_v9mip/. The OCO-2 and ObsPack data can also be downloaded from https://www.esrl.noaa.gov/gmd/ccgg/OCO2_v9mip/download.php. The growth rate of atmospheric CO_2 mixing ratios is documented at NOAA-ESRL website (https://www.esrl.noaa.gov/gmd/ccgg/trends/gl_gr.html). The CONTRAIL (doi: https://doi.org/10.17595/20180208.001) data for 2015–2016 available publicly as part of the ObsPack data package was used for model evaluation. Tracks of CONTRAIL flights can be accessed here: http://www.cger.nies.go.jp/contrail/fstatis2015.html. NDVI and EVI data were collected from the MODIS instrument on the Terra satellite (MOD13C2 Climate Modeling Grid (CMG) Version 6, https://doi.org/10.5067/MODIS/MOD13C2.006) and AVHRR sensor (doi: https://doi.org/10.7289/V5ZG6QH9). We used SIF data from OCO-2 (SIFoco2_005; doi: https://doi.org/10.3334/ORNLDAAC/1696) and GOME-2 (https://avdc.gsfc.nasa.gov/pub/data/satellite/MetOp/GOME_F/v28/MetOp-B/level3/).

Acknowledgments
Sajeev Philip acknowledges financial support of the NASA Academic Mission Services by Universities Space Research Association at NASA Ames Research Center. Matthew S. Johnson acknowledges the internal funding from NASA's Earth Science Research and Analysis Program. Nuggehalli K. Indira would like to thank IFCPAR (Indo-French Centre for the Promotion of Advanced Research), CSIR (Council of Scientific and Industrial Research, India), and DST (Department of Science and Technology, India) for funding the measurements. Computing resources supporting this work were provided by the NASA High-End Computing Program through the NASA Advanced Supercomputing Division at NASA Ames Research Center. We thank the OCO-2 Science Team for providing the version 9 OCO-2 product. We also thank the OCO-2 Flux Inversion Team, GEOS-Chem model developers, and MsTMIP project team members (https://doi.org/10.3334/ORNLDAAC/1315), for the free availability of their products. CarbonTracker CT2019 fluxes were provided by National Oceanographic and Atmospheric Administration's Earth System Research Laboratory, Boulder, Colorado, USA from the website at http://carbontracker.noaa.gov. The MODIS NDVI and EVI Level 3 (MOD13C2 Climate Modeling Grid (CMG) Version 6) data were acquired from doi:10.5067/MODIS/MOD13C2.006. The NOAA Climate Data Record AVHRR NDVI (Version 5 product) CDR was acquired from NOAA's National Centers for Environmental Information (http://www.ncei.noaa.gov). This CDR was originally developed by Eric Vermote and colleagues for NOAA's CDR Program. We acknowledge all data providers to ObsPack data packaged for the OCO-2 v9 MIP. We acknowledge the CONTRAIL project team members for the public availability of their data as part of the ObsPack data package. We are thankful to Andrew Jacobson (ObsPack data and CT2019 fluxes), Tomohiro Oda and Ray Nassar (fossil fuel data), Christopher Potter (NASA-CASA model data), Katherine D. Haynes (SiB-4 model data), and Joanna Joiner (GOME-2 SIF) for sharing data. We also thank Sean Crowell, Andrew Jacobson, Junjie Liu, and Andrew Schuh for fruitful discussions during the OCO-2 Science Team meetings which helped conducting the OCO-2 v9 MIP experiments during this study. The views, opinions, and findings contained in this report are those of the authors and should not be construed as an official NASA or United States Government position, policy, or decision.

References

Baker, D. F., Bell, E., Davis, K. J., Campbell, J. F., Lin, B., & Dobler, J. (2021). A new exponentially-decaying error correlation model for assimilating OCO-2 column-average CO2 data, using a length scale computed from airborne lidar measurements. *Geoscientific Model Development Discussions*. [preprint]. https://doi.org/10.5194/gmd-2020-444

Baker, D. F., Bösch, H., Doney, S. C., O'Brien, D., & Schimel, D. S. (2010). Carbon source/sink information provided by column CO_2 measurements from the Orbiting Carbon Observatory. *Atmospheric Chemistry and Physics*, *10*(9), 4145–4165. https://doi.org/10.5194/acp-10-4145-2010

Ballantyne, A., Alden, C., Miller, J., Tans, P. P., & White, J. W. C. (2012). Increase in observed net carbon dioxide uptake by land and oceans during the past 50 years. *Nature*, *488*, 70–72. https://doi.org/10.1038/nature11299

Bastos, A., Friedlingstein, P., Sitch, S., Chen, C., Mialon, A., Wigneron, J.-P., et al. (2018). Impact of the 2015/2016 El Niño on the terrestrial carbon cycle constrained by bottom-up and top-down approaches. *Philosophical Transactions of the Royal Society B*, *373*, 20170304. https://doi.org/10.1098/rstb.2017.0304

Bastos, A., O'Sullivan, M., Ciais, P., Makowski, D., Sitch, S., Friedlingstein, P., et al. (2020). Sources of uncertainty in regional and global terrestrial CO_2 exchange estimates. *Global Biogeochemical Cycles*, *34*, e2019GB006393. https://doi.org/10.1029/2019GB006393

Basu, S., Baker, D. F., Chevallier, F., Patra, P. K., Liu, J., & Miller, J. B. (2018). The impact of transport model differences on CO_2 surface flux estimates from OCO-2 retrievals of column average CO_2. *Atmospheric Chemistry and Physics*, *18*(10), 7189–7215. https://doi.org/10.5194/acp-18-7189-2018

Basu, S., Guerlet, S., Butz, A., Houweling, S., Hasekamp, O., Aben, I., et al. (2013). Global CO_2 fluxes estimated from GOSAT retrievals of total column CO_2. *Atmospheric Chemistry and Physics*, *13*(17), 8695–8717. https://doi.org/10.5194/acp-13-8695-2013

Basu, S., Krol, M., Butz, A., Clerbaux, C., Sawa, Y., Machida, T., et al. (2014). The seasonal variation of the CO_2 flux over Tropical Asia estimated from GOSAT, CONTRAIL, and IASI. *Geophysical Research Letters*, *41*(5), 1809–1815. https://doi.org/10.1002/2013gl059105

Bey, I., Jacob, D. J., Yantosca, R. M., Logan, J. A., Field, B. D., Fiore, A. M., et al. (2001). Global modeling of tropospheric chemistry with assimilated meteorology: Model description and evaluation. *Journal of Geophysical Research*, *106*(D19), 23073–23095. https://doi.org/10.1029/2001jd000807

Bhattacharya, S. K., Borole, D. V., Francey, R. J., Allison, C. E., Steele, L. P., Krummel, P., et al. (2009). Trace gases and CO_2 isotope records from Cabo de Rama, India. *Current Science*, *97*, 1336–1344. https://www.jstor.org/stable/24109728

Bousserez, N., Henze, D. K., Perkins, A., Bowman, K. W., Lee, M., Liu, J., et al. (2015). Improved analysis-error covariance matrix for high-dimensional variational inversions: Application to source estimation using a 3D atmospheric transport model. *The Quarterly Journal of the Royal Meteorological Society*, *141*, 1906–1921. https://doi.org/10.1002/qj.2495

Bowman, K. W., Liu, J., Bloom, A. A., Parazoo, N. C., Lee, M., Jiang, Z., et al. (2017). Global and Brazilian carbon response to El Niño Modoki 2011–2010. *Earth and Space Science*, *4*(10), 637–660. https://doi.org/10.1002/2016ea000204

Braswell, B. H., Schimel, D. S., Linder, E., & Moore, B., III. (1997). The response of global terrestrial ecosystems to interannual temperature variability. *Science*, *278*, 870–873. https://doi.org/10.1126/science.278.5339.870

Brenninkmeijer, C. A. M., Crutzen, P., Boumard, F., Dauer, T., Dix, B., Ebinghaus, R., et al. (2007). Civil Aircraft for the regular investigation of the atmosphere based on an instrumented container: The new CARIBIC system. *Atmospheric Chemistry and Physics*, *7*, 4953–4976. https://doi.org/10.5194/acp-7-4953-2007

Byrne, B., Jones, D. B. A., Strong, K., Zeng, Z.-C., Deng, F., & Liu, J. (2017). Sensitivity of CO_2 surface flux constraints to observational coverage. *Journal of Geophysical Research: Atmospheres*, *122*(12), 6672–6694. https://doi.org/10.1002/2016jd026164

Carbontracker Team. (2019). *Compilation of near real time atmospheric carbon dioxide data; obspack_co2_1_NRT_v5.0_2019-08-13*. NOAA Earth System Research Laboratory, Global Monitoring Division. https://doi.org/10.25925/20190813

Cervarich, M., Shu, S., Jain, A. K., Arneth, A., Canadell, J., Friedlingstein, P., et al. (2016). The terrestrial carbon budget of South and Southeast Asia. *Environmental Research Letters*, *11*, 105006. https://doi.org/10.1088/1748-9326/11/10/105006

Chakraborty, S., Tiwari, Y. K., Burman, P. K. D., Roy, S. B., & Valsala, V. (2020). Observations and modeling of GHG concentrations and fluxes over India. In R. Krishnan, J. Sanjay, C. Gnanaseelan, M. Mujumdar, A. Kulkarni, & S. Chakraborty (Eds.), *Assessment of climate change over the Indian region* (pp. 73–92). Springer. https://doi.org/10.1007/978-981-15-4327-2_4

Chevallier, F., Ciais, P., Conway, T. J., Aalto, T., Anderson, B. E., Bousquet, P., et al. (2010). CO_2 surface fluxes at grid point scale estimated from a global 21 year reanalysis of atmospheric measurements. *Journal of Geophysical Research*, *115*, D21307. https://doi.org/10.1029/2010jd013887

Ciais, P., Bastos, A., Chevallier, F., Lauerwald, R., Poulter, B., Canadell, P., et al. (2021). Definitions and methods to estimate regional land carbon fluxes for the second phase of the REgional Carbon Cycle Assessment and Processes Project (RECCAP-2). *Geoscientific Model Development Discussions*. [preprint]. https://doi.org/10.5194/gmd-2020-259

Ciais, P., Dolman, A. J., Bombelli, A., Duren, R., Peregon, A., Rayner, P. J., et al. (2014). Current systematic carbon-cycle observations and the need for implementing a policy-relevant carbon observing system. *Biogeosciences*, *11*(13), 3547–3602. https://doi.org/10.5194/bg-11-3547-2014

Ciais, P., Rayner, P., Chevallier, F., Bousquet, P., Logan, M., Peylin, P., & Ramonet, M. (2010). Atmospheric inversions for estimating CO_2 fluxes: Methods and perspectives. *Climatic Change*, *103*(1–2), 69–92. https://doi.org/10.1007/s10584-010-9909-3

Ciais, P., Yao, Y., Gasser, T., Baccini, A., Wang, Y., Lauerwald, R., et al. (2020). Empirical estimates of regional carbon budgets imply reduced global soil heterotrophic respiration. *National Science Review*, *8*, 1–14. https://doi.org/10.1093/nsr/nwaa145

Crisp, D., Pollock, H. R., Rosenberg, R., Chapsky, L., Lee, R. A. M., Oyafuso, F. A., et al. (2017). The on-orbit performance of the Orbiting Carbon Observatory-2 (OCO-2) instrument and its radiometrically calibrated products. *Atmospheric Measurement Techniques*, *10*, 59–81. https://doi.org/10.5194/amt-10-59-2017

Crowell, S., Baker, D., Schuh, A., Basu, S., Jacobson, A. R., Chevallier, F., et al. (2019). The 2015–2016 carbon cycle as seen from OCO-2 and the global in situ network. *Atmospheric Chemistry and Physics*, *19*, 9797–9831. https://doi.org/10.5194/acp-19-9797-2019

Deng, F., Jones, D. B. A., Henze, D. K., Bousserez, N., Bowman, K. W., Fisher, J. B., et al. (2014). Inferring regional sources and sinks of atmospheric CO_2 from GOSAT XCO_2 data. *Atmospheric Chemistry and Physics*, *14*(7), 3703–3727. https://doi.org/10.5194/acp-14-3703-2014

Denning, A. S., Collatz, G. J., Zhang, C., Randall, D. A., Berry, J. A., Sellers, P. J., et al. (1996). Simulations of terrestrial carbon metabolism and atmospheric CO_2 in a general circulation model. *Tellus B: Chemical and Physical Meteorology*, *48*(4), 521–542. https://doi.org/10.3402/tellusb.v48i4.15930

Eldering, A., Wennberg, P. O., Crisp, D., Schimel, D. S., Gunson, M. R., Chatterjee, A., et al. (2017). The Orbiting Carbon Observatory-2 early science investigations of regional carbon dioxide fluxes. *Science*, *358*, eaam5745. https://doi.org/10.1126/science.aam5745

Fisher, J. B., Sikka, M., Huntzinger, D. N., Schwalm, C., & Liu, J. (2016). Technical note: 3-hourly temporal downscaling of monthly global terrestrial biosphere model net ecosystem exchange. *Biogeosciences*, *13*(14), 4271–4277. https://doi.org/10.5194/bg-13-4271-2016

Fisher, J. B., Sikka, M., Huntzinger, D. N., Schwalm, C. R., Liu, J., Wei, Y., et al. (2016). *CMS: Modeled net ecosystem exchange at 3-hourly time steps, 2004–2010*. ORNL DAAC. https://doi.org/10.3334/ORNLDAAC/1315

Frankenberg, C., Drewry, D., Geier, S., Verma, M., Lawson, P., Stutz, J., & Grossmann, K. (2016). Remote sensing of solar induced chlorophyll fluorescence from satellites, airplanes and ground-based stations. In *Geoscience and Remote Sensing Symposium (IGARSS), 2016 IEEE International* (pp. 1707–1710). https://doi.org/10.1109/IGARSS.2016.7729436

Friedlingstein, P., Jones, M. W., O'Sullivan, M., Andrew, R. M., Hauck, J., Peters, G. P., et al. (2019). Global carbon budget 2019. *Earth System Science Data*, *11*(4), 1783–1838. https://doi.org/10.5194/essd-11-1783-2019

Friedlingstein, P., Meinshausen, M., Arora, V. K., Jones, C. D., Anav, A., Liddicoat, S. K., & Knutti, R. (2014). Uncertainties in CMIP5 climate projections due to carbon cycle feedbacks. *Journal of Climate*, *27*, 511–526. https://doi.org/10.1175/jcli-d-12-00579.1

Friedlingstein, P., O'Sullivan, M., Jones, M. W., Andrew, R. M., Hauck, J., Olsen, A., et al. (2020). Global carbon budget 2020. *Earth System Science Data*, *12*(4), 3269–3340. https://doi.org/10.5194/essd-12-3269-2020

Gahlot, S., Shu, S., Jain, A. K., & Roy, S. B. (2017). Estimating trends and variation of net biome productivity in India for 1980–2012 using a land surface model. *Geophysical Research Letters*, *44*, 11573–11579. https://doi.org/10.1002/2017GL075777

Gaubert, B., Stephens, B. B., Basu, S., Chevallier, F., Deng, F., Kort, E. A., et al. (2019). Global atmospheric CO_2 inverse models converging on neutral tropical land exchange, but disagreeing on fossil fuel and atmospheric growth rate. *Biogeosciences*, *16*, 117–134. https://doi.org/10.5194/bg-16-117-2019

Giglio, L., Randerson, J. T., & van der Werf, G. R. (2013). Analysis of daily, monthly, and annual burned area using the fourth-generation global fire emissions database (GFED4). *Journal of Geophysical Research: Biogeosciences*, *118*(1), 317–328. https://doi.org/10.1002/jgrg.20042

Giglio, L., van der Werf, G. R., Randerson, J. T., Collatz, G. J., & Kasibhatla, P. (2006). Global estimation of burned area using MODIS active fire observations. *Atmospheric Chemistry and Physics*, *6*(4), 957–974. https://doi.org/10.5194/acp-6-957-2006

Gurney, K. R., Law, R. M., Denning, A. S., Rayner, P. J., Baker, D., Bousquet, P., et al. (2002). Towards robust regional estimates of annual mean CO_2 sources and sinks. *Nature*, *415*, 626–630. https://doi.org/10.1038/415626a

Haynes, K. D., Baker, I. T., Denning, A. S., Stöckli, R., Schaefer, K., Lokupitiya, E. Y., & Haynes, J. M. (2019). Representing grass lands using dynamic prognostic phenology based on biological growth stages: 1. Implementation in the simple biosphere model (SiB4). *Journal of Advances in Modeling Earth Systems*, *11*, 4423–4439. https://doi.org/10.1029/2018MS001540

Henze, D. K., Hakami, A., & Seinfeld, J. H. (2007). Development of the adjoint of GEOS-Chem. *Atmospheric Chemistry and Physics*, *7*, 2413–2433. https://doi.org/10.5194/acp-7-2413-2007

Houweling, S., Baker, D., Basu, S., Boesch, H., Butz, A., Chevallier, F., et al. (2015). An intercomparison of inverse models for estimating sources and sinks of CO_2 using GOSAT measurements. *Journal of Geophysical Research: Atmospheres*, *120*(10), 5253–5266. https://doi.org/10.1002/2014jd022962

Huete, A., Didan, K., Miura, T., Rodriguez, E. P., Gao, X., & Ferreira, L. G. (2002). Overview of the radiometric and biophysical performance of the MODIS vegetation indices. *Remote Sensing of Environment*, *83*(1–2), 195–213. https://doi.org/10.1016/s0034-4257(02)00096-2

Huntzinger, D. N., Schwalm, C., Michalak, A. M., Schaefer, K., King, A. W., Wei, Y., et al. (2013). The North American Carbon Program Multi-scale synthesis and Terrestrial Model Intercomparison Project—Part 1: Overview and experimental design. *Geoscientific Model Development*, *6*(6), 2121–2133. https://doi.org/10.5194/gmd-6-2121-2013

Huntzinger, D. N., Schwalm, C. R., Wei, Y., Cook, R. B., Michalak, A. M., Schaefer, K., et al. (2018). *NACP MsTMIP: Global 0.5-degree model outputs in standard format, version 1.0*. ORNL DAAC. https://doi.org/10.3334/ORNLDAAC/1225

Jacobson, A. R., Mikaloff Fletcher, S. E., Gruber, N., Sarmiento, J. L., & Gloor, M. (2007). A joint atmosphere-ocean inversion for surface fluxes of carbon dioxide: 1. Methods and global-scale fluxes. *Global Biogeochemical Cycles*, *21*, GB1019. https://doi.org/10.1029/2005GB002556

Jacobson, A. R., Schuldt, K. N., Miller, J. B., Oda, T., Tans, P., Andrews, A., et al. (2020). *CarbonTracker CT2019*. Retrieved from https://gml.noaa.gov/ccgg/carbontracker/CT2019_doc.php

Jethva, H., Torres, O., Field, R. D., Lyapustin, A., Gautam, G., & Kayetha, V. (2019). Connecting crop productivity, residue fires, and air quality over Northern India. *Scientific Reports*, *9*, 16594. https://doi.org/10.1038/s41598-019-52799-x

Jiang, F., Wang, H. M., Chen, J. M., Machida, T., Zhou, L. X., Ju, W. M., et al. (2014). Carbon balance of China constrained by CONTRAIL aircraft CO_2 measurements. *Atmospheric Chemistry and Physics*, *14*(18), 10133–10144. https://doi.org/10.5194/acp-14-10133-2014

Joiner, J., Guanter, L., Lindstrot, R., Voigt, M., Vasilkov, A. P., Middleton, E. M., et al. (2013). Global monitoring of terrestrial chlorophyll fluorescence from moderate-spectral-resolution near-infrared satellite measurements: Methodology, simulations, and application to GOME-2. *Atmospheric Measurement Techniques*, *6*, 2803–2823. https://doi.org/10.5194/amt-6-2803-2013

Joiner, J., Yoshida, Y., Guanter, L., & Middleton, E. M. (2016). New methods for the retrieval of chlorophyll red fluorescence from hyperspectral satellite instruments: Simulations and application to GOME-2 and SCIAMACHY. *Atmospheric Measurement Techniques*, *9*(8), 3939–3967. https://doi.org/10.5194/amt-9-3939-2016

Joiner, J., Yoshida, Y., Vasilkov, A. P., Schaefer, K., Jung, M., Guanter, L., et al. (2014). The seasonal cycle of satellite chlorophyll fluorescence observations and its relationship to vegetation phenology and ecosystem atmosphere carbon exchange. *Remote Sensing of Environment*, *152*, 375–391. https://doi.org/10.1016/j.rse.2014.06.022

Kiel, M., O'Dell, C. W., Fisher, B., Eldering, A., Nassar, R., MacDonald, C. G., & Wennberg, P. O. (2019). How bias correction goes wrong: Measurement of XCO_2 affected by erroneous surface pressure estimates. *Atmospheric Measurement Techniques*, *12*(4), 2241–2259. https://doi.org/10.5194/amt-12-2241-2019

Kondo, M., Patra, P. K., Sitch, S., Friedlingstein, P., Poulter, B., Chevallier, F., et al. (2020). State of the science in reconciling top-down and bottom-up approaches for terrestrial CO_2 budget. *Global Change Biology*, *26*, 1068–1084. https://doi.org/10.1111/gcb.14917

Krishnapriya, M., Nayak, R. K., Allahudeen, S., Bhuvanachandra, A., Dadhwal, V. K., Jha, C. S., et al. (2020). Seasonal variability of tropospheric CO_2 over India based on model simulation, satellite retrieval and in-situ observation. *Journal of Earth System Science*, *129*(1), 211. https://doi.org/10.1007/s12040-020-01478-x

Lin, X., Ciais, P., Bousquet, P., Ramonet, M., Yin, Y., Balkanski, Y., et al. (2018). Simulating CH_4 and CO_2 over South and East Asia using the zoomed chemistry transport model LMDz-INCA. *Atmospheric Chemistry and Physics*, *18*(13), 9475–9497. https://doi.org/10.5194/acp-18-9475-2018

Lin, X., Indira, N. K., Ramonet, M., Delmotte, M., Ciais, P., Bhatt, B. C., et al. (2015). Long-lived atmospheric trace gases measurements in flask samples from three stations in India. *Atmospheric Chemistry and Physics*, *15*, 9819–9849. https://doi.org/10.5194/acp-15-9819-2015

Liu, J., Bowman, K. W., Lee, M., Henze, D. K., Bousserez, N., Brix, H., et al. (2014). Carbon monitoring system flux estimation and attribution: Impact of ACOS-GOSAT XCO_2 sampling on the inference of terrestrial biospheric sources and sinks. *Tellus B: Chemical and Physical Meteorology*, *66*, 22486. https://doi.org/10.3402/tellusb.v66.22486

Liu, J., Bowman, K. W., Schimel, D. S., Parazoo, N. C., Jiang, Z., Lee, M., et al. (2017). Contrasting carbon cycle responses of the tropical continents to the 2015–2016 El Niño. *Science*, *358*, eaam5690. https://doi.org/10.1126/science.aam5690

Luus, K. A., Commane, R., Parazoo, N. C., Benmergui, J., Euskirchen, E. S., Frankenberg, C., et al. (2017). Tundra photosynthesis captured by satellite-observed solar-induced chlorophyll fluorescence. *Geophysical Research Letters*, *44*, 1564–1573. https://doi.org/10.1002/2016gl070842

Machida, T., Matsueda, H., Sawa, Y., Nakagawa, Y., Hirotani, K., Kondo, N., et al. (2008). Worldwide measurements of atmospheric CO_2 and other trace gas species using commercial airlines. *Journal of Atmospheric and Oceanic Technology*, *25*, 1744–1754. https://doi.org/10.1175/2008JTECHA1082.1

Masarie, K. A., Peters, W., Jacobson, A. R., & Tans, P. P. (2014). ObsPack: A framework for the preparation, delivery, and attribution of atmospheric greenhouse gas measurements. *Earth System Science Data*, *6*, 375–384. https://doi.org/10.5194/essd-6-375-2014

Miller, S. M., & Michalak, A. M. (2020). The impact of improved satellite retrievals on estimates of biospheric carbon balance. *Atmospheric Chemistry and Physics*, *20*, 323–331. https://doi.org/10.5194/acp-20-323-2020

Mu, M., Randerson, J. T., van der Werf, G. R., Giglio, L., Kasibhatla, P., Morton, D., et al. (2011). Daily and 3-hourly variability in global fire emissions and consequences for atmospheric model predictions of carbon monoxide. *Journal of Geophysical Research: Atmospheres*, *116*, D24303. https://doi.org/10.1029/2011jd016245

Nalini, K., Sijikumar, S., Valsala, V., Tiwari, Y. K., & Ramachandran, R. (2019). Designing surface CO_2 monitoring network to constrain the Indian land fluxes. *Atmospheric Environment*, *218*, 117003. https://doi.org/10.1016/j.atmosenv.2019.117003

Nalini, K., Uma, K. N., Sijikumar, S., Tiwari, Y. K., & Ramachandran, R. (2018). Satellite- and ground-based measurements of CO_2 over the Indian region: Its seasonal dependencies, spatial variability, and model estimates. *International Journal of Remote Sensing*, *39*(22), 7881–7900. https://doi.org/10.1080/01431161.2018.1479787

Nassar, R., Jones, D. B. A., Suntharalingam, P., Chen, J. M., Andres, R. J., Wecht, K. J., et al. (2010). Modeling global atmospheric CO_2 with improved emission inventories and CO_2 production from the oxidation of other carbon species. *Geoscientific Model Development*, *3*(2), 689–716. https://doi.org/10.5194/gmd-3-689-2010

Nassar, R., Napier-Linton, L., Gurney, K. R., Andres, R. J., Oda, T., Vogel, F. R., & Deng, F. (2013). Improving the temporal and spatial distribution of CO_2 emissions from global fossil fuel emission data sets. *Journal of Geophysical Research: Atmospheres*, *118*(2), 917–933. https://doi.org/10.1029/2012jd018196

Nayak, R. K., Patel, N. R., & Dadhwal, V. K. (2015). Spatio-temporal variability of net ecosystem productivity over India and its relationship to climatic variables. *Environmental Earth Sciences*, *74*, 1743–1753. https://doi.org/10.1007/s12665-015-4182-4

Newsam, G. N., & Enting, I. G. (1988). Inverse problems in atmospheric constituent studies. I. Determination of surface sources under a diffusive transport approximation. *Inverse Problems*, *4*, 1037–1054. https://doi.org/10.1088/0266-5611/4/4/008

Niwa, Y., Machida, T., Sawa, Y., Matsueda, H., Schuck, T. J., Brenninkmeijer, C. A. M., et al. (2012). Imposing strong constraints on tropical terrestrial CO_2 fluxes using passenger aircraft based measurements. *Journal of Geophysical Research: Atmospheres*, *117*, D11303. https://doi.org/10.1029/2012jd017474

Oda, T., Maksyutov, S., & Andres, R. J. (2018). The Open-Source Data Inventory for Anthropogenic CO_2, version 2016 (ODIAC2016): A global monthly fossil fuel CO_2 gridded emissions data product for tracer transport simulations and surface flux inversions. *Earth System Science Data*, *10*, 87–107. https://doi.org/10.5194/essd-10-87-2018

O'Dell, C. W., Connor, B., Bösch, H., O'Brien, D., Frankenberg, C., Castano, R., et al. (2012). The ACOS CO_2 retrieval algorithm—Part 1: Description and validation against synthetic observations. *Atmospheric Measurement Techniques*, *5*(1), 99–121. https://doi.org/10.5194/amt-5-99-2012

O'Dell, C. W., Eldering, A., Wennberg, P. O., Crisp, D., Gunson, M. R., Fisher, B., et al. (2018). Improved retrievals of carbon dioxide from Orbiting Carbon Observatory-2 with the version 8 ACOS algorithm. *Atmospheric Measurement Techniques*, *11*(12), 6539–6576. https://doi.org/10.5194/amt-11-6539-2018

Olsen, S. C., & Randerson, J. T. (2004). Differences between surface and column atmospheric CO_2 and implications for carbon cycle research. *Journal of Geophysical Research: Atmospheres*, *109*, D02301. https://doi.org/10.1029/2003jd003968

Palmer, P. I., Feng, L., Baker, D., Chevallier, F., Bösch, H., & Somkuti, P. (2019). Net carbon emissions from African biosphere dominate pan-tropical atmospheric CO_2 signal. *Nature Communications*, *10*, 3344. https://doi.org/10.1038/s41467-019-11097-w

Patra, P. K., Canadell, J. G., Houghton, R. A., Piao, S. L., Oh, N.-H., Ciais, P., et al. (2013). The carbon budget of South Asia. *Biogeosciences*, *10*, 513–527. https://doi.org/10.5194/bg-10-513-2013

Patra, P. K., Crisp, D., Kaiser, J. W., Wunch, D., Saeki, T., Ichii, K., et al. (2017). The Orbiting Carbon Observatory (OCO-2) tracks 2–3 peta-gram increase in carbon release to the atmosphere during the 2014–2016 El Niño. *Scientific Reports*, *7*(1), 13567. https://doi.org/10.1038/s41598-017-13459-0

Patra, P. K., Niwa, Y., Schuck, T. J., Brenninkmeijer, C. A. M., Machida, T., Matsueda, H., & Sawa, Y. (2011). Carbon balance of South Asia constrained by passenger aircraft CO_2 measurements. *Atmospheric Chemistry and Physics*, *11*(9), 4163–4175. https://doi.org/10.5194/acp-11-4163-2011

Peiro, H., Crowell, S., Schuh, A., Baker, D. F., O'Dell, C., Jacobson, A. R., et al. (2021). Four years of global carbon cycle observed from OCO-2 version 9 and in situ data, and comparison to OCO-2 v7. *Atmospheric Chemistry and Physics Discussions*. https://doi.org/10.5194/acp-2021-373

Peters, G. P., Andrew, R. M., Canadell, J. G., Friedlingstein, P., Jackson, R. B., Korsbakken, J. I., et al. (2020). Carbon dioxide emissions continue to grow amidst slowly emerging climate policies. *Nature Climate Change*, *10*, 3–6. https://doi.org/10.1038/s41558-019-0659-6

Peters, W., Jacobson, A. R., Sweeney, C., Andrews, A. E., Conway, T. J., Masarie, K., et al. (2007). An atmospheric perspective on North American carbon dioxide exchange: CarbonTracker. *Proceedings of the National Academy of Sciences of the United States of America*, *104*, 18925–18930. https://doi.org/10.1073/pnas.0708986104

Peylin, P., Law, R. M., Gurney, K. R., Chevallier, F., Jacobson, A. R., Maki, T., et al. (2013). Global atmospheric carbon budget: Results from an ensemble of atmospheric CO_2 inversions. *Biogeosciences*, *10*(10), 6699–6720. https://doi.org/10.5194/bg-10-6699-2013

Philip, S., Johnson, M. S., Potter, C., Genovesse, V., Baker, D. F., Haynes, K. D., et al. (2019). Prior biosphere model impact on global terrestrial CO_2 fluxes estimated from OCO-2 retrievals. *Atmospheric Chemistry and Physics*, *19*(20), 13267–13287. https://doi.org/10.5194/acp-19-13267-2019

Potter, C., Klooster, S., & Genovese, V. (2012). Net primary production of terrestrial ecosystems from 2000 to 2009. *Climatic Change*, *115*, 365–378. https://doi.org/10.1007/s10584-012-0460-2

Potter, C., Klooster, S., Genovese, V., Hiatt, C., Boriah, S., Kumar, V., et al. (2012). Terrestrial ecosystem carbon fluxes predicted from MODIS satellite data and large-scale disturbance modeling. *International Journal of Geosciences*, *3*(3), 469–479. https://doi.org/10.4236/ijg.2012.33050

Potter, C., Klooster, S., Huete, A., Genovese, V., Bustamante, M., Guimaraes Ferreira, L., et al. (2009). Terrestrial carbon sinks in the Brazilian Amazon and Cerrado region predicted from MODIS satellite data and ecosystem modeling. *Biogeosciences*, *6*, 937–945. https://doi.org/10.5194/bg-6-937-2009

Potter, C., Klooster, S., Myneni, R., Genovese, V., Tan, P.-N., & Kumar, V. (2003). Continental scale comparisons of terrestrial carbon sinks estimated from satellite data and ecosystem modeling 1982–1998. *Global and Planetary Change*, *39*(3–4), 201–213. https://doi.org/10.1016/j.gloplacha.2003.07.001

Potter, C., Kumar, V., Klooster, S., & Nemani, R. (2007). Recent history of trends in vegetation greenness and large-scale ecosystem disturbances in Eurasia. *Tellus B: Chemical and Physical Meteorology*, *59*(2), 260–272. https://doi.org/10.1111/j.1600-0889.2006.00245.x

Potter, C., Randerson, J. T., Field, C. B., Matson, P. A., Vitousek, P. M., Mooney, H. A., & Klooster, S. A. (1993). Terrestrial ecosystem production: A process model based on global satellite and surface data. *Global Biogeochemical Cycles*, *7*, 811–841. https://doi.org/10.1029/93GB02725

Poulter, B., Frank, D., Ciais, P., Myneni, R. B., Andela, N., Bi, J., et al. (2014). Contribution of semi-arid ecosystems to interannual variability of the global carbon cycle. *Nature*, *509*, 600–603. https://doi.org/10.1038/nature13376

Randerson, J. T., Thompson, M. V., Malmstrom, C. M., Field, C. B., & Fung, I. Y. (1996). Substrate limitations for heterotrophs: Implications for models that estimate the seasonal cycle of atmospheric CO_2. *Global Biogeochemical Cycles*, *10*, 585–602. https://doi.org/10.1029/96GB01981

Rao, A. S., Bala, G., Ravindranath, N. H., & Nemani, R. (2019). Multi-model assessment of trends, variability and drivers of terrestrial carbon uptake in India. *Journal of Earth System Science*, *128*, 99. https://doi.org/10.1007/s12040-019-1120-y

Ravi Kumar, R., Valsala, V., Tiwari, Y. K., Revadekar, J. V., Pillai, P., Chakraborty, S., & Murtugudde, R. (2016). Intra-seasonal variability of atmospheric CO_2 concentrations over India during summer monsoons. *Atmospheric Environment*, *142*, 229–237. https://doi.org/10.1016/j.atmosenv.2016.07.023

Rayner, P. J., & O'Brien, D. M. (2001). The utility of remotely sensed CO_2 concentration data in surface source inversions. *Geophysical Research Letters*, *28*(1), 175–178. https://doi.org/10.1029/2000gl011912

Schimel, D. S., House, J. I., Hibbard, K. A., Bousquet, P., Ciais, P., Peylin, P., et al. (2001). Recent patterns and mechanisms of carbon exchange by terrestrial ecosystems. *Nature*, *414*, 169–172. https://doi.org/10.1038/35102500

Schimel, D. S., Stephens, B. B., & Fisher, J. B. (2015). Effect of increasing CO_2 on the terrestrial carbon cycle. *Proceedings of the National Academy of Sciences of the United States of America*, *112*, 436–441. https://doi.org/10.1073/pnas.1407302112

Schuck, T. J., Brenninkmeijer, C. A. M., Baker, A. K., Slemr, F., von Velthoven, P. F. J., & Zahn, A. (2010). Greenhouse gas relationships in the Indian summer monsoon plume measured by the CARIBIC passenger aircraft. *Atmospheric Chemistry and Physics*, *10*(8), 3965–3984. https://doi.org/10.5194/acp-10-3965-2010

Schuh, A. E., Jacobson, A. R., Basu, S., Weir, B., Baker, D., Bowman, K., et al. (2019). Quantifying the impact of atmospheric transport uncertainty on CO_2 surface flux estimates. *Global Biogeochemical Cycles*, *33*, 484–500. https://doi.org/10.1029/2018GB006086

Sellers, P. J., Mintz, Y., Sud, Y. C., & Dalcher, A. (1986). A simple biosphere model (SiB) for use within general circulation models. *Journal of the Atmospheric Sciences*, *43*, 505–531. https://doi.org/10.1175/1520-0469(1986)043<0505:ASBMFU>2.0.CO;2

Shiga, Y. P., Tadić, J. M., Qiu, X., Yadav, V., Andrews, A. E., Berry, J. A., & Michalak, A. M. (2018). Atmospheric CO_2 observations reveal strong correlation between regional net biospheric carbon uptake and solar-induced chlorophyll fluorescence. *Geophysical Research Letters*, *45*, 1122–1132. https://doi.org/10.1002/2017GL076630

Sitch, S., Friedlingstein, P., Gruber, N., Jones, S. D., Murray-Tortarolo, G., Ahlström, A., et al. (2015). Recent trends and drivers of regional sources and sinks of carbon dioxide. *Biogeosciences*, *12*, 653–679. https://doi.org/10.5194/bg-12-653-2015

Sitch, S., Smith, B., Prentice, I. C., Arneth, A., Bondeau, A., Cramer, W., et al. (2003). Evaluation of ecosystem dynamics, plant geography and terrestrial carbon cycling in the LPJ dynamic global vegetation model. *Global Change Biology*, *9*, 161–185. https://doi.org/10.1046/j.1365-2486.2003.00569.x

Sreenivas, G., Mahesh, P., Biswadip, G., Suresh, S., Rao, P. V. N., Chaitanya, M. K., & Srinivasulu, P. (2019). Spatio-temporal distribution of CO_2 mixing ratio over Bhubaneswar, Varanasi and Jodhpur of India– airborne campaign, 2016. *Atmospheric Environment*, *201*, 257–264. https://doi.org/10.1016/j.atmosenv.2019.01.010

Sun, Y., Frankenberg, C., Jung, M., Joiner, J., Guanter, L., Köhler, P., & Magney, T. (2018). Overview of solar-induced chlorophyll fluorescence (SIF) from the Orbiting Carbon Observatory-2: Retrieval, cross-mission comparison, and global monitoring for GPP. *Remote Sensing of Environment*, *209*, 808–823. https://doi.org/10.1016/j.rse.2018.02.016

Sun, Y., Frankenberg, C., Wood, J. D., Schimel, D. S., Jung, M., Guanter, L., et al. (2017). OCO-2 advances photosynthesis observation from space via solar-induced chlorophyll fluorescence. *Science*, *358*, eaam5747. https://doi.org/10.1126/science.aam5747

Suntharalingam, P., Jacob, D. J., Palmer, P. I., Logan, J. A., Yantosca, R. M., Xiao, Y., et al. (2004). Improved quantification of Chinese carbon fluxes using CO_2/CO correlations in Asian outflow. *Journal of Geophysical Research: Atmospheres*, *109*, D18S18. https://doi.org/10.1029/2003jd004362

Swathi, P. S., Indira, N. K., & Ramonet, M. (2021). Estimation of carbon dioxide fluxes between land, ocean and atmosphere during 2006-2011 with a 4D variational assimilation scheme and special reference to Asia. In M. Goel, T. Satyanarayana, & D. P. Agrawal (Eds.), *Estimation of carbon dioxide fluxes between land, ocean and atmosphere during 2006–2011 with a 4-D variational assimilation scheme and special reference to Asia, climate change and green chemistry of CO_2 sequestration* (pp. 289–310). Springer. https://doi.org/10.1007/978-981-16-0029-6_17

Thompson, R. L., Patra, P. K., Chevallier, F., Maksyutov, S., Law, R. M., Ziehn, T., et al. (2016). Top-down assessment of the Asian carbon budget since the mid 1990s. *Nature Communications*, *7*, 10724. https://doi.org/10.1038/ncomms10724

Tiwari, Y. K., Revadekar, J. V., & Ravi Kumar, K. (2013). Variations in atmospheric carbon dioxide and its association with rainfall and vegetation over India. *Atmospheric Environment*, *68*, 45–51. https://doi.org/10.1016/j.atmosenv.2012.11.040

Tiwari, Y. K., Valsala, V., Vellore, R. K., & Kunchala, R. K. (2013). Effectiveness of surface monitoring stations in representing regional CO_2 emissions over India. *Climate Research*, *56*(2), 121–129. https://doi.org/10.3354/cr01149

Tiwari, Y. K., Vellore, R. K., Ravi Kumar, K., van der Schoot, M., & Cho, C.-H. (2014). Influence of monsoons on atmospheric CO_2 spatial variability and ground-based monitoring over India. *The Science of the Total Environment*, *490*, 570–578. https://doi.org/10.1016/j.scitotenv.2014.05.045

Tucker, C. J., Fung, I. Y., Keeling, C. D., & Gammon, R. H. (1986). Relationship between atmospheric CO_2 variations and a satellite-derived vegetation index. *Nature*, *319*, 195–199. https://doi.org/10.1038/319195a0

Umezawa, T., Matsueda, H., Sawa, Y., Niwa, Y., Machida, T., & Zhou, L. (2018). Seasonal evaluation of tropospheric CO_2 over the Asia-Pacific region observed by the CONTRAIL commercial airliner measurements. *Atmospheric Chemistry and Physics*, *18*(20), 14851–14866. https://doi.org/10.5194/acp-18-14851-2018

Valsala, V., Tiwari, Y. K., Pillai, P., Roxy, M., Maksyutov, S., & Murtugudde, R. (2013). Intraseasonal variability of terrestrial biospheric CO_2 fluxes over India during summer monsoons. *Journal of Geophysical Research: Biogeosciences*, *118*(2), 752–769. https://doi.org/10.1002/jgrg.20037

van der Werf, G. R., Randerson, J. T., Collatz, G. J., & Giglio, L. (2003). Carbon emissions from fires in tropical and subtropical ecosystems. *Global Change Biology*, *9*(4), 547–562. https://doi.org/10.1046/j.1365-2486.2003.00604.x

van der Werf, G. R., Randerson, J. T., Collatz, G. J., Giglio, L., Kasibhatla, P. S., Arellano, A. F., et al. (2004). Continental-scale partitioning of fire emissions during the 1997 to 2001 El Nino/La Nina period. *Science*, *303*, 73–76. https://doi.org/10.1126/science.1090753

van der Werf, G. R., Randerson, J. T., Giglio, L., Collatz, G. J., Kasibhatla, P. S., & Arellano, A. F., Jr. (2006). Interannual variability in global biomass burning emissions from 1997 to 2004. *Atmospheric Chemistry and Physics*, *6*(11), 3423–3441. https://doi.org/10.5194/acp-6-3423-2006

van der Werf, G. R., Randerson, J. T., Giglio, L., Collatz, G. J., Mu, M., Kasibhatla, P. S., et al. (2010). Global fire emissions and the contribution of deforestation, savanna, forest, agricultural, and peat fires (1997–2009). *Atmospheric Chemistry and Physics*, *10*(23), 11707–11735. https://doi.org/10.5194/acp-10-11707-2010

van der Werf, G. R., Randerson, J. T., Giglio, L., van Leeuwen, T. T., Chen, Y., Rogers, B. M., et al. (2017). Global fire emissions estimates during 1997–2016. *Earth System Science Data*, *9*(2), 697–720. https://doi.org/10.5194/essd-9-697-2017

Venkataraman, C., Habib, G., Eiguren-Fernandez, A., Miguel, A. H., & Fiedlander, S. K. (2005). Residential biofuels in South Asia: Carbonaceous aerosols emissions and climate impacts. *Science*, *307*, 1454–1456. https://doi.org/10.1126/science.1104359

Vermote, E. F. (2019). *NOAA CDR Program, NOAA climate data Record (CDR) of AVHRR normalized difference vegetation index (NDVI), version 5*. NOAA National Centers for Environmental Information. https://doi.org/10.7289/V5ZG6QH9

Vermote, E. F., & Kotchenova, S. (2008). Atmospheric correction for the monitoring of land surfaces. *Journal of Geophysical Research*, *113*, D23S90. https://doi.org/10.1029/2007JD009662

Villalobos, Y., Rayner, P. J., Silver, J. D., Thomas, S., Haverd, V., Knauer, J., et al. (2021). Was Australia a sink or source of CO2 in 2015? Data assimilation using OCO-2 satellite measurements. *Atmospheric Chemistry and Physics*, *21*(23), 17453–17494. https://doi.org/10.5194/acp-21-17453-2021

Wang, H., Jiang, F., Wang, J., Ju, W., & Chen, J. M. (2019). Terrestrial ecosystem carbon flux estimated using GOSAT and OCO-2 XCO_2 retrievals. *Atmospheric Chemistry and Physics*, *19*(18), 12067–12082. https://doi.org/10.5194/acp-19-12067-2019

Yu, L., Wen, J., Chang, C. Y., Frankenberg, C., & Sun, Y. (2019a). *High resolution global contiguous SIF estimates derived from OCO-2 SIF and MODIS*. ORNL DAAC. https://doi.org/10.3334/ORNLDAAC/1696

Yu, L., Wen, J., Chang, C. Y., Frankenberg, C., & Sun, Y. (2019b). High resolution global contiguous SIF of OCO-2. *Geophysical Research Letters*, *46*, 1449–1458. https://doi.org/10.1029/2018gl081109